Enhancement of hydrogen evolution activity by tailoring the electronic structure in ruthenium-heteroatom-doped cobalt iron phosphide nanoframes

Kunik Jang [a],[1], Hyunseok Yoon [a],[1], Ji Seong Hyoung [a], Dwi Sakti Aldianto Pratama [b], Chan Woo Lee [b], Dong-Wan Kim [a],[*]

[a] School of Civil, Environmental and Architectural Engineering, Korea University, Seoul 02841, the Republic of Korea
[b] Department of Chemistry, Kookmin University, Seoul 02707, the Republic of Korea

ARTICLE INFO

ABSTRACT

Designing cost-effective and highly efficient electrocatalysts for hydrogen evolution reaction (HER) in alkaline media at high current densities is challenging. In this study, we adopted Ru heteroatom doping and an open nanoframe structure to obtain excellent HER catalytic performance. X-ray photoelectron spectroscopy (XPS) visualized the electron transfer due to Ru heteroatom doping in transition metal phosphides, to observe the modulated electronic structure of the Ru-doped CoFeP nanoframe (RCFP/NF). Density functional theory (DFT) calculations and XPS analysis confirmed a D-band center downshift of the RCFP/NF, demonstrating the regulation of the optimal adsorbates (OH*/H*) adsorption free energies. Consequently, RCFP/NF with 4.7 wt % of Ru exhibits a low overpotential of 112 mV, 191 mV, and 219 mV at current densities of 10 mA cm^{-2}, 100 mA cm^{-2}, and 500 mA cm^{-2}, respectively, and an excellent stability for 100 h at a high current density of 100 mA cm^{-2}. This outstanding HER performance at high current density was attributed to the hydrophilic and aerophobic properties of the RCFP/NF catalyst surface that facilitate the exposure of active sites and H$_2$ gas desorption.

1. Introduction

Green hydrogen produced by water electrolysis is a clean and sustainable energy source that has attracted considerable attention as an alternative to traditional fossil fuels to mitigate environmental issues [1]. However, the large energy consumption during large-scale hydrogen production, which is attributed to the sluggish hydrogen evolution reaction (HER) kinetics in alkaline media, reduces the energy conversion efficiency [2]. Although Pt-based catalysts exhibit excellent electrocatalytic performance in the HER, their cost, scarcity, and instability in alkaline media restrict their widespread application in large-scale hydrogen production [3–5]. Therefore, the development of HER electrocatalysts that are both cost-effective and abundant in nature is crucial to replace Pt-based electrocatalysts.

Recently, various transition metal phosphides (TMPs) have revealed great potential as Pt-free electrocatalysts, such as FeP, CoP, Ni$_2$P, MoP, etc [6–8]. Advanced bimetallic phosphides have emerged as highly active HER electrocatalysts because of their modified electronic structures. In particular, cobalt-iron bimetallic phosphide (CoFeP) exhibits superior HER activity than both CoP and FeP because of its higher conductivity and moderate hydrogen adsorption energy [9,10]. Additionally, the incorporation of Fe into the CoP lattice improves the structural stability and lowers the degradation of CoFeP during the HER. However, further progress towards higher catalytic activity is necessary to obtain more efficient catalysts.

Modifying the electronic structure of TMPs is a promising strategy for enhancing their catalytic performance [11]. Heteroatom doping with different electronegativities has been demonstrated to efficiently induce charge transfer, which regulates the water dissociation and OH*/H* adsorption energies on the catalyst surface [12]. Among various metal dopants, Ru, which possesses a suitable OH*/H* adsorption energy, facilitates water dissociation and exhibits moderate Ru-H binding energy similar to Pt-H [13]. In addition, Ru doping can contribute to optimizing the electronic structures of the active sites of TMPs by inducing charge transfer and modulating the electron density distribution, thereby improving the intrinsic activity. For instance, Zhai et al.

[14] reported that Ru single-atom doping not only provided Ru active sites with favorable H* adsorption energy, but also regulated the H* adsorption energy at the Ni and Fe sites of Ru-doped NiFe layered double hydroxides. Moreover, Qu et al. [15] synthesized Ru-doped NiFeP nanosheets on Ni foam and demonstrated that Ru doping improved the electrocatalytic activity at P sites.

Owing to their intriguing inherent properties, metal-organic frameworks (MOFs) have been widely used as catalysts [16–18]. Three-dimensional (3D) nanostructured MOFs with open frameworks provide large surface areas and pathways for electrons and reactants [19,20]. Additional exposure to the active sites inside the structure can enhance the catalytic activity of electrocatalytic materials. Furthermore, open frameworks facilitate charge and mass transfer, resulting in the improvement of the catalytic reaction kinetics compared to solid structures [21]. Recently, Prussian blue analogs (PBAs) with high structural stabilities have been reported as precursors of efficient catalysts for water splitting [17,22,23].

In this study, we designed a Ru-doped cobalt-iron phosphide nanoframe (RCFP/NF)-structured HER electrocatalyst using a CoFe PBA nanoframe (CoFe PBA/NF) open-framework template. After Ru ion exchange and subsequent phosphorization, the as-prepared RCFP/NF maintained its original nanoframe structure, exposing numerous active sites and facilitating mass transfer. Meanwhile, the cyanide group (-CN-) in PBA was converted into an N, P co-doped carbon layer encapsulating the nanoparticles during phosphorization, which enhanced the catalytic activity and stability. To elucidate the electronic structural changes during the synthesis process, X-ray photoelectron spectroscopy (XPS) was used to analyze each synthesis step. Density functional theory (DFT) calculations confirmed that a small amount of Ru doping in the CoFeP nanoframe (CFP/NF) contributes to the improvement of the intrinsic activity of the alkaline HER by reducing the adsorbates (OH*/H*) adsorption energy. In addition, various properties such as excellent intrinsic activity, high electrochemical surface area (ECSA), and fast mass transfer capability are required to achieve superior HER performance under high current densities, for practical mass hydrogen production. The fabricated RCFP/NF met all these requirements and exhibited excellent HER performance with a very low overpotential of 219 mV at a high current density of 500 mA cm^{-2}. Furthermore, the synthesized RCFP/NF was operated at 100 mA cm^{-2} for more than 100 h without significant degradation, indicating its high stability under alkaline HER conditions. In conclusion, our study demonstrates that the combination of electronic modulation by Ru doping, the subsequent phosphorization, and the unique open nanoframe structure of RCFP/NF synergistically enhance the HER performance.

2. Experimental section

2.1. Materials

Cobalt (II) acetate tetrahydrate (Co(CH$_3$COO)$_2$·4H$_2$O, 98 %), potassium hexacyanoferrate (III) (K$_3$[Fe(CN)$_6$], 99 %), and ruthenium chloride hydrate (RuCl$_3$·xH$_2$O) were purchased from Sigma-Aldrich. Sodium hypophosphite monohydrate (NaH$_2$PO$_2$·H$_2$O), trisodium citrate dihydrate (Na$_3$C$_6$H$_5$O$_7$·2H$_2$O, 99 %), and commercial Pt/C (20 wt %) were obtained from Alfa Aesar.

2.2. Synthesis of CoFe PBA/NFs and CoFe PBA nanocubes (CoFe PBA/NCs)

CoFe PBA/NF was synthesized using a chemical precipitation method. 264 mg (0.8 mmol) of potassium hexacyanoferrate (III) was dissolved in 120 mL of deionized (DI) water to obtain solution A. 300 mg (1.2 mmol) of cobalt (II) acetate tetrahydrate and 294 mg (1.0 mmol) of trisodium citrate dihydrate were also dissolved in 80 mL of DI water to form solution B. Then, solution B was added into solution A for 15 s under vigorous magnetic stirring. After stirring for 5 min, the solution

was aged at 80 ℃ in an electric oven for 6 h. A violet precipitate was collected by centrifugation, washed with DI water and ethanol more than three times and vacuum dried at 60 ℃ overnight.

Nanoframes of different sizes were synthesized using a similar method by changing the time taken to add solution B to A. The feeding time was varied from 3 to 160 s (3, 7, 15, 30, 80, and 160 s), and the smallest- and largest-sized samples correspond to 3 and 160 s, respectively, and were denoted as CoFe PBA-small/NF and CoFe PBA-large/NF. Additionally, CoFe PBA-small/NC, CoFe PBA-medium/NC, and CoFe PBA-large/NC were synthesized according to the same process as CoFe PBA-small/NF, CoFe PBA/NF, and CoFe PBA-large/NF but without the precipitation procedure.

2.3. Synthesis of Ru-doped CoFe PBA nanoframes (Ru-CoFe PBA/NFs)

60 mg of the CoFe PBA/NF was dispersed in 25 mL of DI water under ultrasonication for 10 min. At the same time, 7.5 mg of RuCl$_3$·xH$_2$O were dispersed in 10 mL of DI water via the same procedure. Then, RuCl$_3$ aqueous solution was added to the CoFe PBA/NF solution slowly at 60 ℃ under 300 rpm stirring, and the mixture was further stirred for 2 h. Afterward, the obtained Ru-CoFe PBA/NF was washed with DI water and ethanol, and freeze dried. To compare the effects of Ru, Ru-CoFe PBA/NFs with different Ru content were synthesized by adjusting the amount of Ru (0, 2.5, 5.0, 7.5, 10.0, 15.0, and 20 mg).

2.4. Synthesis of RCFP/NF and CFP/NF

The prepared Ru-CoFe PBA/NF and NaH$_2$PO$_2$ powders were placed in two separate positions in a tube furnace. 150 mg of NaH$_2$PO$_2$ powder was placed at the center of the tube, and 15 mg of Ru-CoFe PBA/NFs was placed 7 cm downstream from the center. The furnace was heated to 500 ℃ for 2 h with a rate of 2 ℃ min^{-1}, under an Ar atmosphere (100 sccm). Subsequently, the obtained metal phosphide sample was cooled to room temperature and named as RCFP/NF. For comparison, the CFP/NF sample was synthesized using the same phosphorization process, but the CoFe PBA/NF precursor was used without Ru ion exchange.

2.5. Synthesis of Ru-doped CoFeP nanocube (RCFP/NC)

For morphological comparison, the prepared CoFe PBA-large/NC with a particle size distribution similar to that of CoFe PBA/NF was used in the same Ru ion exchange process as Ru-CoFe PBA/NF and denoted as Ru-CoFe PBA-large/NC. Consequently, the Ru-CoFe PBA-large/NC was heated using the same phosphorization process as RCFP/NF and named RCFP/NC.

2.6. Synthesis of CoFe (CF), Ru-CoFe (RCF), P doped RCF alloys/NF and alloy-driven Ru-doped CoFeP nanoframe (a-RCFP/NF)

30 mg of the above prepared Ru-CoFe PBA/NF was reduced at 300 ℃ for 2 h at a heating rate of 2 ℃ min^{-1} under a mixed gas flow of H$_2$ (10 sccm) and Ar gases (90 sccm). The resulting product, denoted as the RCF alloy/NF, was subsequently heated with NaH$_2$PO$_2$ powder to the same position as the aforementioned metal phosphides. 15 mg of the RCF/NF and 150 mg of the NaH$_2$PO$_2$ powders were heated to 250 and 500 ℃, respectively, at a rate of 2 ℃ min^{-1} for 2 h. The products were denoted as P-doped RCF alloy/NF and a-RCFP/NF. For comparison, CF alloy/NF was synthesized using the CoFe PBA/NF precursor via the same heat treatment as the RCF alloy/NF. Alloy-driven CoFeP nanoframe (a-CFP/NF) was also synthesized using the CF alloy/NF with the same phosphorization as the a-RCFP/NF.

2.7. Characterization

The morphologies were verified using field-emission scanning electron microscopy (FE-SEM; Hitachi, SU-70). Field-emission transmission

electron microscopy (FE-TEM; JEM-F200, JEOL) and energy-dispersive X-ray spectroscopy (EDS) were used to analyze the microstructure and elemental distribution. The crystalline phase was acquired from X-ray diffraction (XRD; Rigaku, MiniFlex 600 diffractometer) patterns using Cu-Kα radiation. An XPS (Nexsa, Thermo Fisher) with Al-Kα radiation was used to investigate the electronic structure of the catalyst surface. The D-band center for the valence band spectra is calculated using the formula, $\frac{\int N(\varepsilon)\varepsilon d\varepsilon}{\int N(\varepsilon)d\varepsilon}$, in the range of 0–8.0 eV, where $N(\varepsilon)$ is the density of states. Electron paramagnetic resonance (EPR) spectra were recorded using a JEOL JES-FA200 electron spin resonance (ESR) spectrometer. The cyanide groups were characterized using Fourier-transform infrared (FTIR) spectroscopy (Cary 630 FTIR, Agilent Technologies, USA). Raman spectroscopy (HEDA, WEVE) was used to examine the d- and g-bands of the carbon layer. The K, Co, Fe, Ru, and P contents were determined by inductively coupled plasma-optical emission spectrometry (ICP-OES; iCAP 7400 DUO, Thermo Scientific) and -mass spectrometry (ICP-MS; iCAP RQ, Thermo Scientific). The surface areas and pore volumes were estimated using the Brunauer-Emmett-Teller (BET) method (BELSORP-max, MicrotracBEL Corp). Static and dynamic contact angles were measured using a pendant-drop tensiometer (DSA100, KURSS). The amount and rate of generated H_2 gas was measured by a gas chromatography (GC) (GC-6890N, Agilent Technologies) equipped with a thermal conductivity detector (TCD) using high-purity Ar as the carrier gas.

2.8. Electrochemical measurement

The electrochemical measurements were performed in a three-electrode cell in an electrochemical workstation (IVIUM Stat). To prepare the working electrode, 3 mg of the catalyst and 60 μL of Nafion solution (Sigma Aldrich, 5 wt %) were dispersed in water/isopropyl alcohol (IPA) solution (740/200 μL) via ultrasonication for 30 min to form a homogeneous ink. Then 10 μL of the dispersed catalyst ink was loaded onto a glassy carbon electrode (GCE) of 5 mm in diameter (loading mass: 0.15 mg cm^{-2}). A Pt plate and Ag/AgCl electrode were used as the counter and reference electrodes, respectively. Prior to the measurement, the Ag/AgCl reference electrode was calibrated with respect to a reversible hydrogen electrode (RHE). A nitrogen-saturated 1.0 M KOH solution (50 mL) was used as the electrolyte at room temperature. Polarization curves were obtained using linear sweep voltammetry (LSV) at a scan rate of 5 mV s^{-1} after several Cyclic voltammetry (CV) scans. During the LSV, the rotation speed of the rotating disk electrode was fixed at 2000 rpm. All reported polarization curves were corrected for ohmic drop and all the potentials were calibrated to RHE according to the following equation:

$E_{RHE} = E_{Ag/AgCl} + 0.210V + 0.0591 \times pH$

Electrochemical impedance spectroscopy (EIS) was conducted in 1.0 M KOH, at a frequency range of 100 kHz to 0.1 Hz and an applied voltage of −1.20 V. CVs in the potential ranges of 0.1–0.3 V and 0.34–0.54 V vs RHE were performed to obtain the double-layer capacitance (C_{dl}) values of CoFe PBA/NFs and metal phosphides, respectively, in non-Faradaic regions. The ECSA of the catalyst was estimated by the following equation:

$ECSA\ [cm^2] = C_{dl}\ [\mu F\ cm^{-2}] * Area\ (geometric)\ [cm^2]\ /C_s\ [\mu F\ cm^{-2}]$

Here, the specific capacitance (C_s) value was assumed to be 40 μF cm^{-2}, as the general value of C_s in 1.0 M KOH is 40 μF cm^{-2} [24–26]. Chronopotentiometry tests at a current density of 100 mA cm^{-2} were conducted for 100 h in a nitrogen-saturated electrolyte, using GCE as a working electrode. Additionally, to observe the morphological and compositional changes of the catalyst after the chronopotentiometry test, the ink was loaded onto a carbon paper (0.5 × 0.5 cm^2), which served as a working electrode for investigating the ex situ XRD, SEM,

and XPS data. Gas chromatography analysis was employed to obtain the Faradaic efficiency. The theoretical amount of generated hydrogen gas and Faradaic efficiency was calculated as the following equation:

$$n\quad [mole]_{theoretically\quad produced} = \frac{Q}{n \times F}$$

$$Faradaic\quad efficiency\quad (\%) = (\frac{n\quad [mole]_{experimentally\quad produced}}{n\quad [mole]_{theoretically\quad produced}}) \times 100$$

Where n [mole] is the mole number of generated hydrogen molecules, Q is the transferred charge, n is the number of electrons participating in HER, and F is Faraday's constant (96,485 C mol^{-1}). The catalyst loaded carbon paper with a geometric area of 2.0 × 2.0 cm^2 was applied as a working electrode to produce a sufficient amount of H_2 gas for GC measurement. The measurement was conducted at a constant current density of 100 mA cm^{-2} and the generated H_2 gas was injected into gas chromatography using 100 μL syringe.

2.9. Computational methods

All spin-polarized DFT calculations were conducted using the Quantum ESPRESSO package in Materials Square [27–29]. The projector-augmented wave (PAW) method represents the elemental core and valence electrons. The electron exchange-correlation interaction was treated within the generalized gradient approximation in the Perdew–Buke–Erznzerhof (GGA-PBE) functional [30]. The van der Waals (vdW) interactions were considered using the Grimme DFT-D3 method. A plane-wave and density cutoffs of 60 and 480 Ry, respectively, were used. The k-sampling point was obtained from the Monkhorst–Pack scheme with a 3×3×1 mesh for optimization and density of states (DOS) calculations. Geometry optimizations were performed with a force convergence smaller than 0.05 eV/A. The CoFeP$_2$ lattice constants (relative errors) were determined to be a = 3.2133 (0.70 %), b = 5.0505 (1.05 %), and c = 5.6234 (0.75 %), which were in good agreement with the experimental results. Subsequently, these bulk parameters were used to construct models for CoFeP$_2$ (111), and a sufficiently large vacuum region of 10 Å was used as spacing between slabs. The half-bottom layers were fixed, and the top layer was free to relax during geometry optimization for each intermediate bond. The free energy ΔG calculation for each step is defined as the difference between the initial and the final states in the following equation:

ΔG = ΔE + ΔZPE – TΔS,

where ΔE, ΔZPE, and ΔS are the binding energy, zero-point energy change, and entropy change, respectively, for each reaction. ZPE and entropy were obtained from reference [31].

3. Results and discussion

3.1. Synthesis and characterization of RCFP/NF catalyst

As schematically shown in Scheme 1, RCFP/NF was synthesized using a three-step process. The first step was to prepare CoFe PBA/NF structures via a co-precipitation reaction. When the three components Co(CH$_3$COO)$_2$·4H$_2$O, K$_3$[Fe(CN)$_6$], and trisodium citrate, which act as chelating agents, were mixed at room temperature for 5 min, CoFe PBA/NCs were formed. To maximize the exposure of the specific surface area, the size of the nanoframe structures was optimized by adjusting the nanocubes to an average size of 200 nm by controlling the feed rate of the sources (Fig. 1a–c and S1). In the following heating stage, the nanoframe nanoparticles were preferentially deposited on the edges and corners of the nanocubes at 80 ℃, as described in Scheme 1. Since the citrate ions selectively capped on the facets of the cubes, the appropriate amount of trisodium citrate served to passivate the facets and expose the reactive edges and corners [32]. Finally, the inner nanocubes were
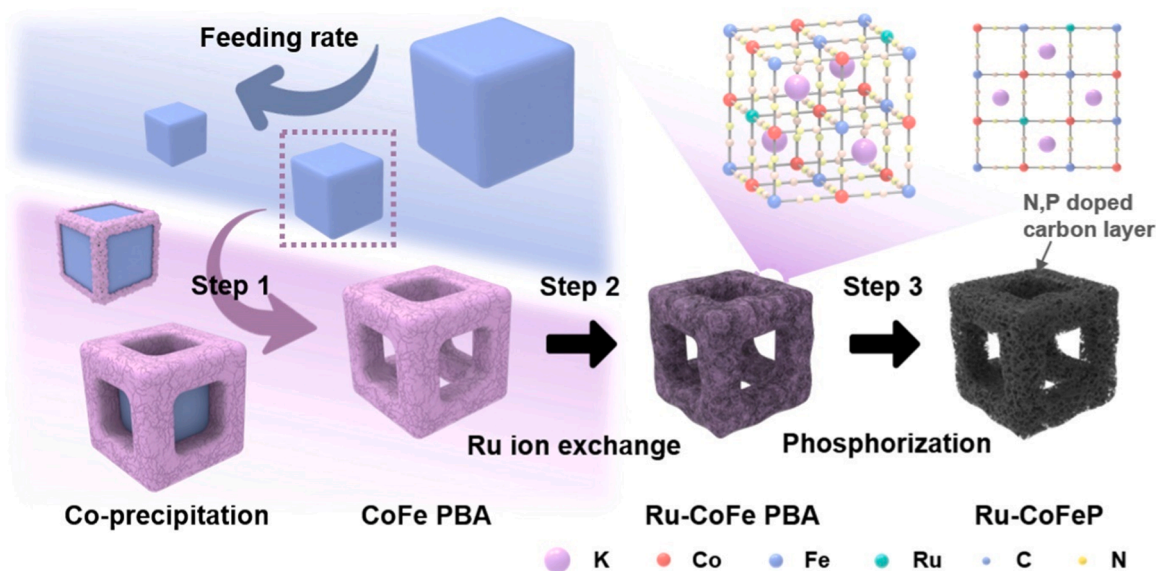
Scheme 1. Schematic illustration of the fabrication of an RCFP/NF.

gradually removed to form the CoFe PBA/NFs (Fig. 1d-f and S2). The morphological formation mechanism of the CoFe PBA/NF was confirmed by SEM images obtained at different precipitation reaction times (Fig. S3). In the XRD patterns in Fig. 1g, the diffraction patterns of the CoFe PBA/NF corresponded to $K_2CoFe(CN)_6$ (PDF #75-0038). The prominent diffraction peaks at 17.7°, 25.1°, and 35.8° were assigned to the (200), (220), and (400) crystal planes of the CoFe PBA/NF. The K/Co/Fe atomic ratio of the CoFe PBA/NF was identified using an ICP-OES, and the verified atomic ratio was approximately 1.0:1.2:1.0 (Table. S1). As confirmed by XRD and ICP-OES analyses, the CoFe PBA/NFs with various particle sizes exhibited the same composition and crystal structure (Fig. 1g and Table. S2). The medium-sized PBA structure had the largest pore volume and specific surface area, as calculated by the BET method, which was in good agreement with the trend of the ECSA (Fig. 1h, S4 and Table. S3). Accordingly, this medium-sized PBA was determined to be the optimal structure for efficiently inducing excellent catalytic behavior.

In the second step, Ru-CoFe PBA/NF was synthesized via a facile Ru ion exchange reaction based on the Kirkendall effect [16]. ICP-OES analysis revealed that Co, Fe, and K in the CoFe PBA/NF participated in the Ru ion exchange reaction, as the contents of each metal decreased with increasing of Ru content (Table. S1). In addition, the decrease in the intensity of the 2p spectra of Co, Fe, and K after Ru ion exchange, observed via XPS, was in good agreement with the ICP-OES results (Fig. 2a–c and S5). Meanwhile, Co 2p and Fe 2p spectra of Ru-CoFe PBA/NF exhibited positive shifts of 0.4 and 0.1 eV in binding energy relative to those of CoFe PBA/NF while the characteristic peaks at 463.5/485.7 eV for Ru 3p, which are slightly lower than peak for Ru^{3+} ions in the benchmark Ru, were assigned to Ru^{3+} [33]. The surface charge redistribution among the metals composing Ru-CoFe PBA/NF indicates that Ru^{3+} ions were successfully incorporated into the cyanide framework [17,34,35]. To further understand the impact of Ru doping on the chemical states of Ru-CoFe PBA/NF, FTIR spectroscopy was conducted (Fig. 2d and S6). By investigating the FTIR spectra, it was observed that the binding structures in the metal cyanide framework changed as the amount of Ru doping increased. The peaks corresponding to the $Co^{II}-N\equiv C-Fe^{II}$ (2073 cm^{-1}) and cyanide complexes with metals in higher oxidation states gradually decreased and increased, respectively, as more Ru was exchanged, suggesting that the doped Ru ions affected the oxidation states of the existing transition metals [36–39]. To observe the effect of Ru exchange on the crystal structure of CoFe PBA/NF, XRD analysis was conducted (Fig. 2e and f). Ru-CoFe PBA/NF showed a

crystal phase similar to that of CoFe PBA/NF, but exhibited a shift toward the high-angle side in proportion to the Ru contents, indicating that the lattice spacings of the PBA structures decreased with Ru doping. Only K$^+$ (164 pm) has a much larger ionic radius than Ru^{3+} (82 pm), implying that the deintercalation of K$^+$ affected the lattice contraction [40,41]. To verify this, Ru-CoFe PBA/NC was synthesized using the CoFe PBA/NC which rarely contains K$^+$ (Table. S4). After an ion-exchange reaction similar to that in Ru-CoFe PBA/NF was performed, no lattice contraction was detected in Ru-CoFe PBA/NC, indicating that the lattice shrinkage of Ru-CoFe PBA/NF was caused by the deintercalation of K$^+$ ions (Fig. S7). According to the magnified peak corresponding to the (200) plane shown in XRD, no further shift was observed when the amount of added Ru source was greater than 15 mg, indicating that additional K$^+$ deintercalation was not detected (Fig. 2f). The ICP-OES analysis revealed that Ru was saturated when the amount of Ru source was 15 mg, and the content of Ru was identified as 7.66 %, which is consistent with the XRD result (Table. S1). TEM image of a Ru-CoFe PBA/NF showed that the nanoframe structures of ~280 nm sizes remained unchanged, and a high-resolution TEM (HRTEM) image with the corresponding selected area electron diffraction (SAED) patterns (inset of Fig. 2h) exhibited the crystalline feature of Ru-CoFe PBA/NF (Fig. 2g and h). In addition, STEM images with the corresponding EDS elemental mapping data indicated that Co, Fe, and Ru were uniformly distributed in the Ru-CoFe PBA/NF, and the Co/Fe/Ru atomic ratio was consistent with the ICP-OES result (Fig. 2i, S8, and Table. S1).

Finally, Ru-CoFe based phosphide was obtained by heat-treatment of Ru-CoFe PBA/NF at 500 °C with NaH$_2$PO$_2$. This synthesis method effectively preserved the original nanoframe structure, denoted as RCFP/NF (Fig. 3a, S9, and S10). The XRD pattern of RCFP/NF showed the diffraction peaks corresponding to CoP (PDF #29–0497), indicating that Co-, Fe-, and even Ru-P represented the unified crystalline phase of orthorhombic CoFeP (Fig. 3b). The small residual peaks of KPO$_3$ (PDF #35–0819) were derived from the remaining potassium. Moreover, no peak shift was observed in XRD with (RCFP/NF) or without (CFP/NF) Ru doping, which implies that the CoP lattice did not change significantly due to similar radii of Ru^0, Co^0, and Fe^0 (i.e., Ru$^{\delta+}$, Co$^{\delta+}$, and Fe$^{\delta+}$) in the orthorhombic crystal structure (i.e., RuP, CoP, and FeP) [22,42,43]. Based on the EDS mapping and line scanning results, Ru, Co, Fe, P, C, and N were uniformly distributed, and the Ru content (4.3 wt %) was confirmed to be very low, which is consistent with the ICP data (Fig. 3c, d, S11–13, and Table. S5). The low Ru content was presumed to be because the Ru exchange process occurred only on the surface, but it was
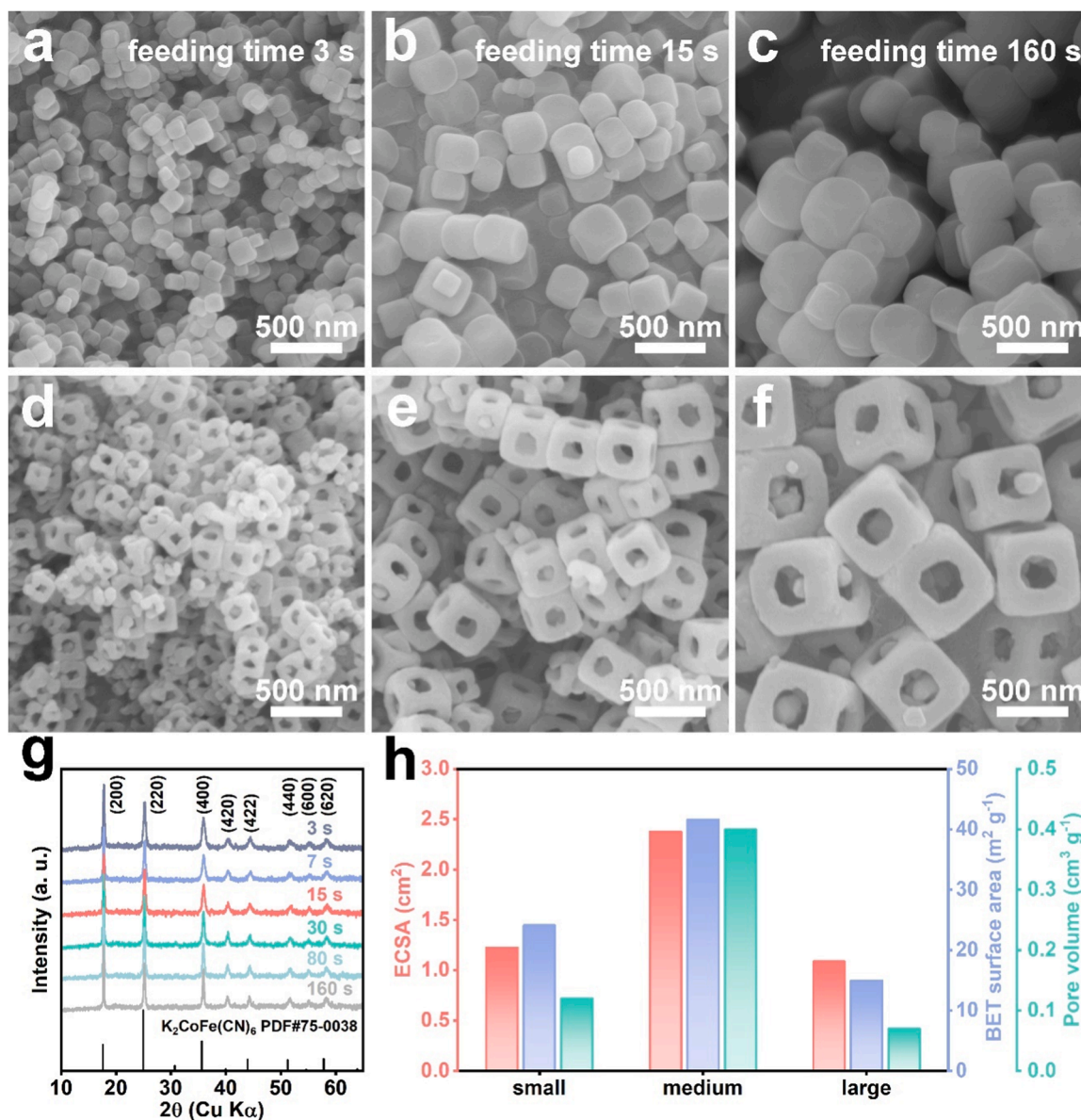
Fig. 1. Size controlling of the CoFe PBA/NF precursor. SEM images of (a) CoFe PBA-small/NC, (b) CoFe PBA-medium/NC, (c) CoFe PBA-large/NC, (d) CoFe PBA-small/NF, (e) CoFe PBA/NF, and (f) CoFe PBA-large/NF. (g) XRD patterns of CoFe PBA/NFs particles with different size distributions by adjusting the feeding time to 3, 7, 15, 30, 80, and 160 s (h) Comparisons of the ECSA evaluated by C_{dl} values, BET surface area, and pore volume of CoFe PBA-small/NF, CoFe PBA/NF, and CoFe PBA-large/NF.

difficult to visually clarify with the EDS elemental mapping images of RCFP/NF because of its thin nanoframe structure. Therefore, the depth of Ru exchange was indirectly confirmed by analyzing the EDS data of the solid RCFP/NC synthesized in the same manner (Figs. 3e, 3f, S14, and Table. S4) [44]. As expected, Ru was found to be thinly distributed only on the edge of the particle, unlike other elements that were evenly distributed inside the particle, because the exchange reaction occurred only on the surface, suggesting that this surface modulation is effective in improving the catalytic activity with a small amount of precious metals. HRTEM images showed that the interplanar distances of 0.190, 0.280, and 0.247 nm were assigned to the (211), (002), and (111) planes in RCFP/NF, respectively (Fig. 3g-i). No intrinsic distortion was detected compared to CFP/NF (0.189, 0.279, and 0.247 nm), which is consistent with the XRD analysis (Fig. 3b and S15). These results imply that the RCFP/NF is composed of ternary solid solution phase of CoP, FeP, and RuP [20,22]. Each nanograin was encapsulated by a thin carbon layer derived from the decomposition of cyano groups (CN⁻) in PBA, as clearly

shown in the HRTEM and EDS images (Fig. 3g-i and S11). According to the EDS quantitative analysis, the carbon layer consisted of C (5.2 wt %) and N (2.0 wt %) contents, indicating the successful formation of N doped carbon layer (Fig. S13). The Raman spectra of RCFP/NF and CFP/NF were obtained to further investigate their graphitic properties (Fig. 3j). The two peaks at 1360 and 1580 cm^{-1} correspond to the D and G bands, respectively, indicating the presence of a carbon layer [45]. Moreover, RCFP/NF exhibited a higher I_D/I_G ratio than CFP/NF, indicating a higher degree of carbon disorder, which promotes electron transport owing to the presence of a higher number of defects on the surface [46,47].

The chemical state of RCFP/NF and the origin of its abundant surface defects were characterized using XPS measurements (Fig. 4a–g). The XPS survey spectra verified RCFP/NF consists of Co, Fe, P, Ru, K, C, N, and O, and as expected, no signals of Ru element were detected in CFP/NF (Fig. 4a). For the Co 2p spectrum of the CFP/NF, the fitted peaks appearing at 778.5 (Co 2p$_{3/2}$) and 793.4 eV (Co 2p$_{1/2}$) were matched to
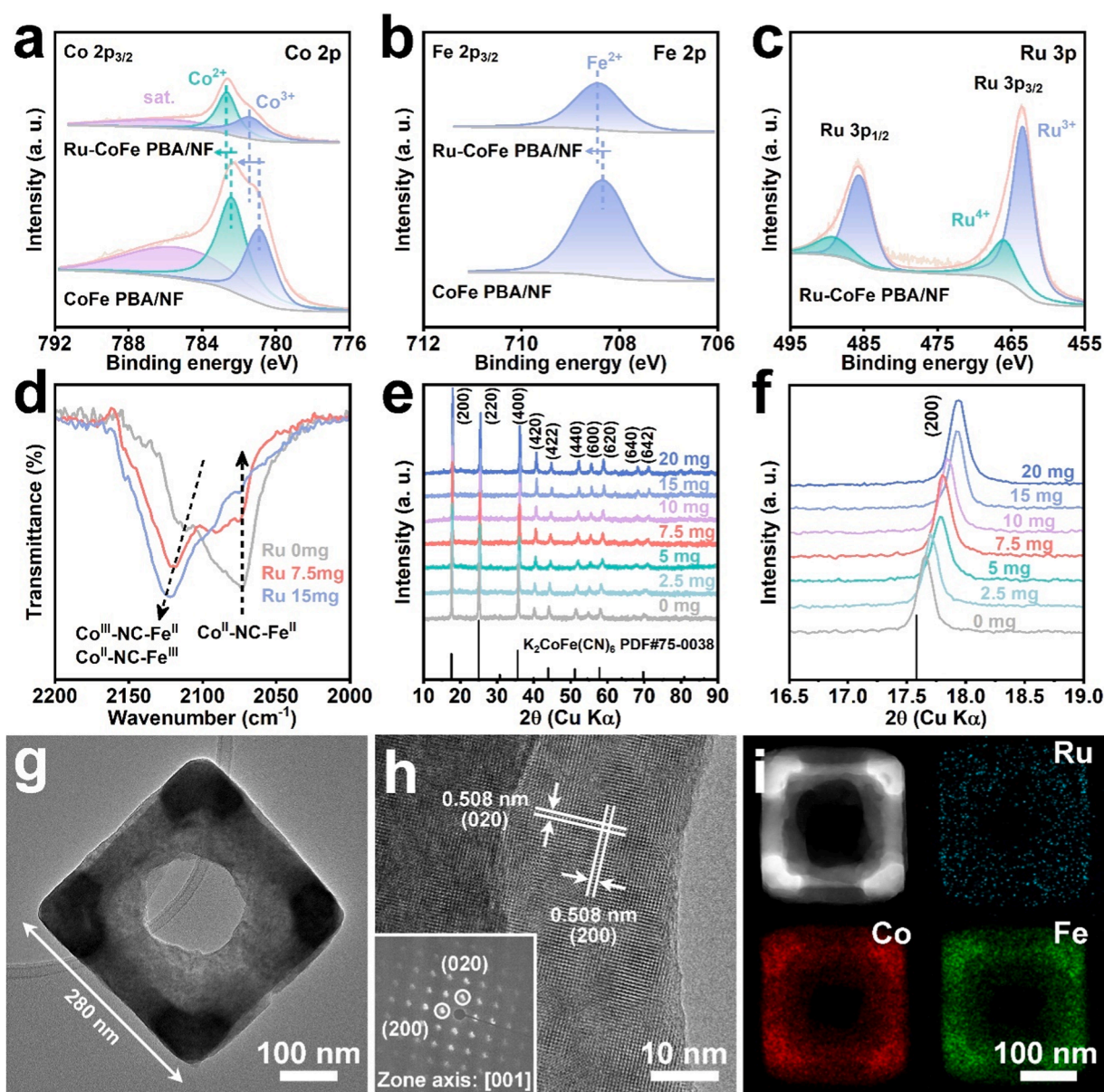
Fig. 2. Compositional and structural characterization of Ru-CoFe PBA/NF. XPS (a) Co 2p, (b) Fe 2p, and (c) Ru 3p spectra of Ru-CoFe PBA/NF and CoFe PBA/NF. (d) FTIR spectra (2000–2200 cm^{-1}) and (e) XRD patterns of Ru-CoFe PBA/NFs with different Ru contents. (f) Magnified (200) peak corresponding to $K_2CoFe(CN)_6$. (g) TEM and (h) HRTEM (inset: corresponding SAED pattern) images of Ru-CoFe PBA/NF. (i) HAADF-STEM image and corresponding EDS mapping of Ru-CoFe PBA/NF, showing Ru (cyan), Co (red), and Fe (green).

Co-P bonds, while the peaks at 781.0, 782.4 (Co $2p_{3/2}$), 796.7, and 797.6 eV (Co $2p_{1/2}$) were attributed to Co-O bonds, and the satellite peaks were observed at 786.0 (Co $2p_{3/2}$) and 802.9 eV (Co $2p_{1/2}$) (Fig. 4b) [22]. Similarly, the peak at 706.9 eV (Fe $2p_{3/2}$) was attributed to the Fe-P bond, and the peaks at 711.4 (Fe $2p_{3/2}$) and 712.7 eV (Fe $2p_{3/2}$), which were ascribed to the Fe-O bond, were accompanied by a satellite peak at 714.3 eV (Fe $2p_{3/2}$) (Fig. 4c) [48]. In the high-resolution P 2p spectra of CFP/NF, the peaks located at 129.1 (P $2p_{3/2}$) and 130.1 eV (P $2p_{1/2}$) were assigned to P-M bonds (M = Co^0, Fe^0). Additionally, another peak at 132.1 eV corresponding to the P-C bond, was attributed to the P doping on the carbon layer, and the other peak at 134.1 eV was consistent with the P-O bond due to inevitable surface oxidation (Fig. 4d) [22,49–51]. Compared to CFP/NF, the binding energy of Co 2p and Fe 2p in RCFP/NF showed a positive shift of 0.6 eV each, and the binding energy of P 2p also exhibited a positive shift of 0.6 eV. Meanwhile, the Ru 3p spectrum of RCFP/NF showed the peaks corresponding to the Ru-P bond at 462.0 (Ru $3p_{1/2}$) and 464.3 eV (Ru

$3p_{3/2}$), and the peaks located at 464.5 (Ru $3p_{1/2}$) and 487.3 eV (Ru $3p_{3/2}$) were indexed to Ru-O bond (Fig. 4e). The binding energy of Ru 3p, which was lower than that of previously reported pristine RuP, revealed strong electronic interactions between Co, Fe, Ru, and P, thus verifying the electronic structure modulation of the active sites in RCFP/NF [52,53]. Moreover, the effect of phosphorization on the electronic structure was confirmed by observing the changes in the XPS spectra from Ru-CoFe PBA/NF to RCFP/NF (Fig. S16). Co, Fe, and Ru of Ru-CoFe PBA/NF were reduced by phosphorization, resulting in peaks corresponding to M-P bonds in Co 2p, Fe 2p, and Ru 3p spectra, indicating the phosphorization significantly regulated the electronic structure along with the Ru doping. The introduction of Ru can reduce the electron density of Co and Fe, thereby facilitating H* adsorption at positively charged Co and Fe sites, while Ru sites with increased electron density can improve the HER performance by regulating the energy required for H_2O dissociation and OH*/H* adsorption [42,43,54]. Moreover, Ru insertion can alleviate the high H* adsorption energy at
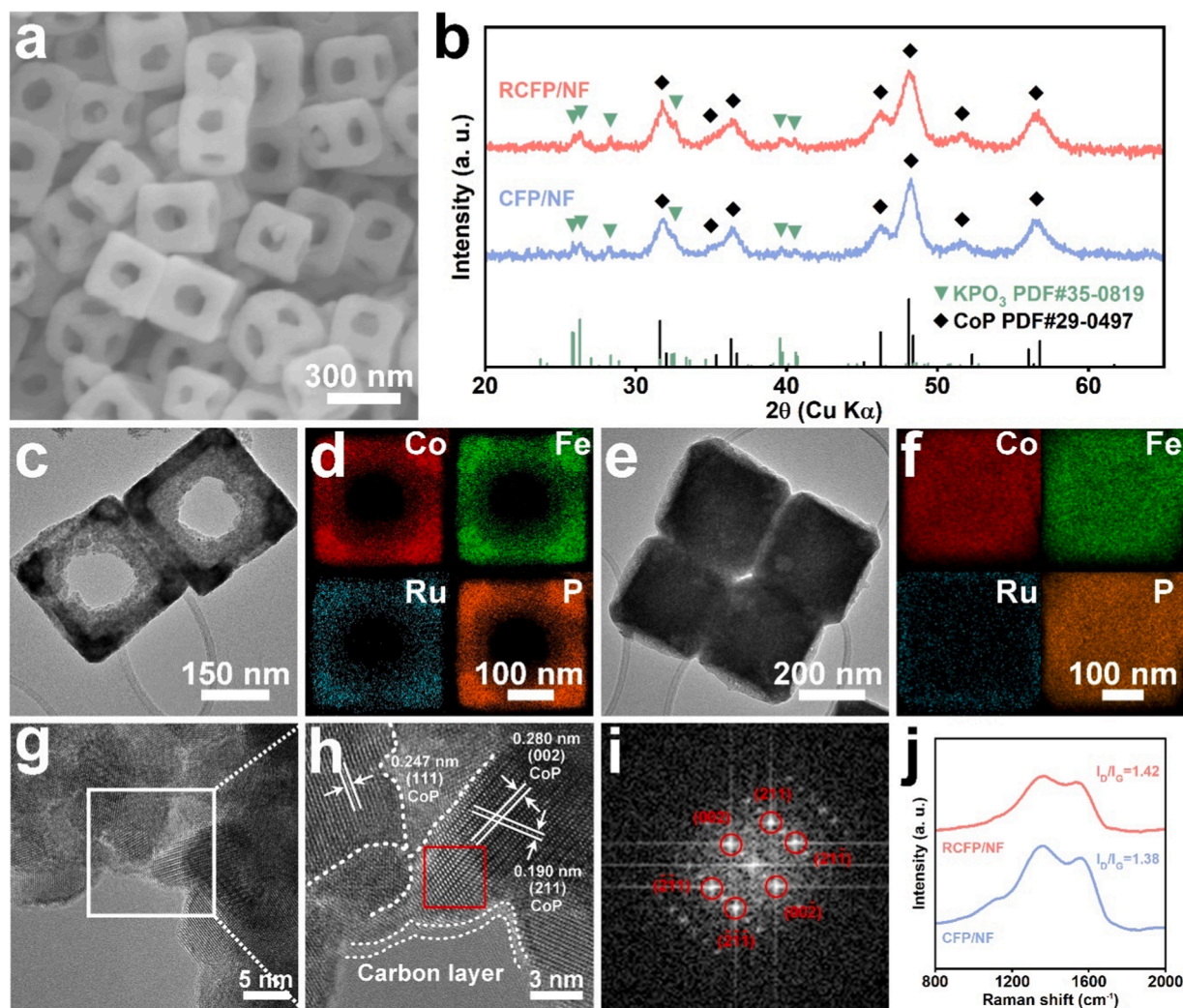
Fig. 3. Synthesis and characterization of RCFP/NF. (a) SEM image of RCFP/NF. (b) XRD patterns of RCFP/NF and CFP/NF. (c) TEM image and (d) corresponding EDS mapping of RCFP/NF. (e) TEM image and (f) corresponding EDS mapping of RCFP/NC. (g, h) HRTEM images and (i) corresponding fast-Fourier-transform (FFT) analysis of RCFP/NF. (j) Raman spectra of RCFP/NF and CFP/NF.

the P active sites by making P less negatively charged than that of CFP/NF [15].

The high-resolution N 1s spectra of RCFP/NF and CFP/NF were deconvoluted into four individual peaks, which were assigned to pyridinic N (398.7 eV), pyrrolic N (400.4 eV), graphitic N (402.8 eV), and oxidized N (407.2 eV) (Fig. 4f). These peaks indicated the successful incorporation of N atoms into the carbon layer and enhanced the electrical conductivity [55–57]. For the C 1 s spectra of the RCFP/NF, the peaks were ascribed to the C-C (284.8 eV), C-P (285.5 eV), C-N/C-O (286.6 eV), and C=O (289.0 eV) bonds (Fig. 4g) [51]. Compared with CFP/NF, the C 1 s and P 2p spectra of the RCFP/NF confirmed the presence of P-C bonds in the carbon layer, which is consistent with the Raman spectra that showed a larger number of defects on the carbon layer surface of RCFP/NF. In addition, the intensities of the M-P bonds in the Co, Fe, and P 2p spectra of the RCFP/NF were stronger than that of the CFP/NF, indicating that the doped Ru present on the surface contributed to the formation of M-P bonds and P-C bonds.

3.2. Synthesis and characterization of RCFP/NF catalyst and mechanism of electron transfer

To investigate the effect of the Ru dopant and phosphorization on the electronic structure in improving the HER catalytic properties of (Co, Fe)-based materials, we characterized the materials at each synthesis

step. For ease of understanding, analyses were performed using metal alloy precursors, from which cyanide anions were rearranged as N-doped carbon shells through a reduction heat treatment (Fig. S17). The reduced alloy precursor adjusted its chemical state to zero valence, to facilitate a better visual understanding. An XPS analysis was performed to trace the electron transfer pathways during the synthesis process (Fig. 5a–d). The XRD patterns of the CF alloy/NF and RCF alloy/NF exhibited diffraction peaks corresponding to the (110), (200), and (211) planes of the CoFe alloy (PDF #49–1568) (Fig. S18). The absence of the diffraction peak of Ru metal in the XRD pattern of the RCF alloy suggests that Ru existed as a solid-solution phase owing to the heteroatom doping of Ru. In addition, no peak shift was detected after Ru doping because the atomic radii of Co, Fe, and Ru were similar. TEM-EDS elemental mapping images revealed a uniform distribution of Co, Fe, and Ru in the RCF alloy/NF, and the ratio of the metal content was confirmed by the ICP-OES results to exhibit the same ratio as the precursor (Ru-CoFe PBA/NF) (Figs. S19, S20, Tables. S1, and S6). The Co 2p XPS spectra showed that the Co^0 peaks of the RCF alloy/NF positively shifted by 0.3 eV compared to that of the CF alloy/NF (Fig. S21). Similarly, the Fe 2p spectra showed a positive shift in the Fe^0 peak after Ru doping. Moreover, the metallic state Ru^0 peaks of the RCF alloy/NF exhibited lower binding energies than previously reported pure Ru metal, indicating electron transfer from Co and Fe to Ru due to the electronegativity gap [58,59].
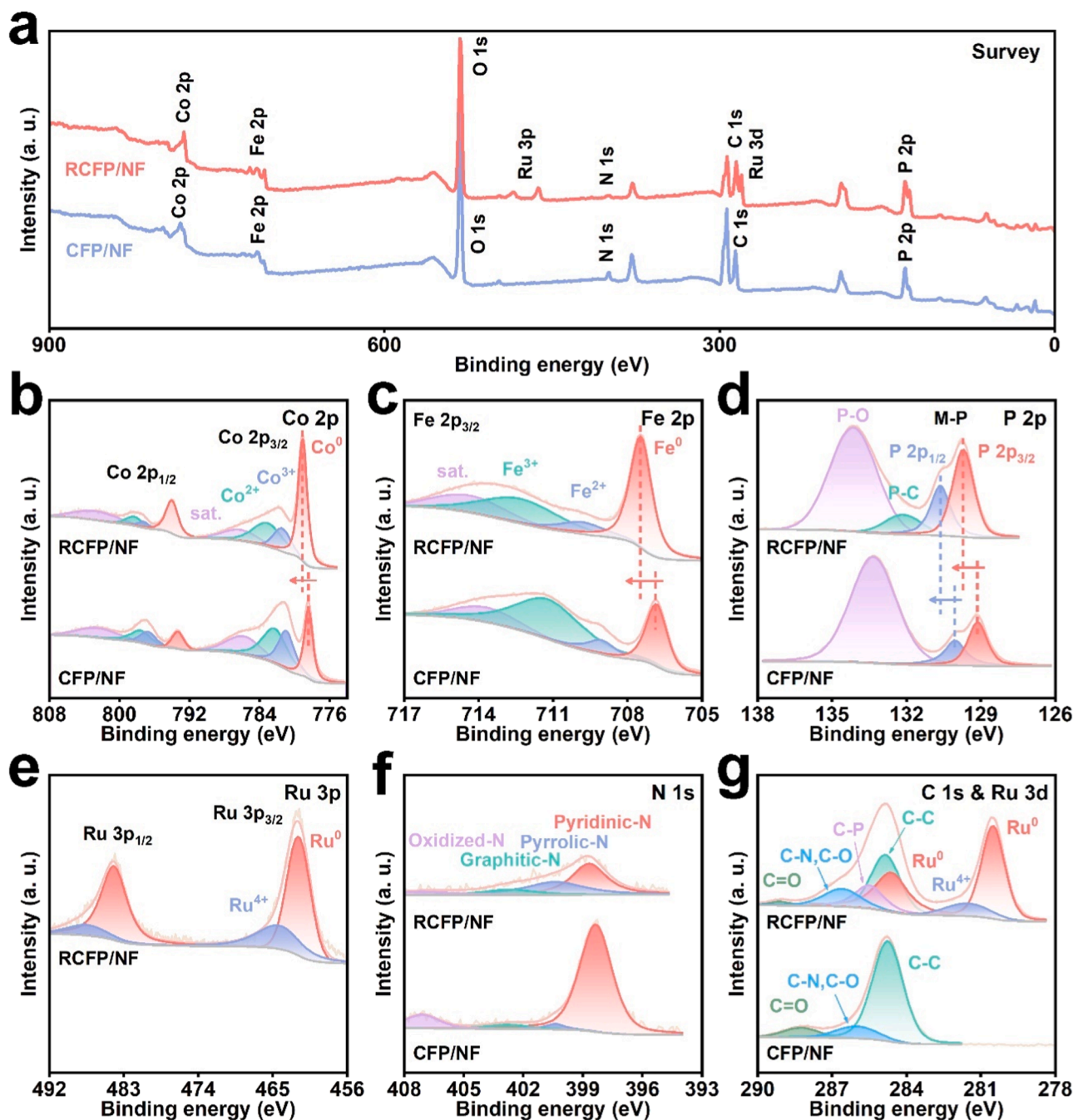
Fig. 4. Electronic structures of RCFP/NF and CFP/NF. XPS (a) survey patterns, (b) Co 2p, (c) Fe 2p, (d) P 2p, (e) Ru 3p, (f) N 1s, and (g) C 1s & Ru 3d spectra of RCFP/NF and CFP/NF.

After Ru doping, the conversion of the alloy precursor to phosphide proceeded in via two-step process: (i) construction of M-P (M = Co, Fe, and Ru) bonds on the surface and (ii) crystalline phase transition into a phosphide. In the first step, the P-doped RCF alloy/NF retained the crystal structure of the RCF alloy/NF, as confirmed by the XRD data (Fig. S18). The P-doped RCF alloy/NF showed a positive shift of 0.2 eV compared to the RCF alloy/NF in the Co 2p and Fe 2p XPS spectra of the Co^0 and Fe^0 peaks, respectively, and no shift was observed in the Ru 3p spectra of the Ru^0 peaks (Fig. 5a–c). The deconvoluted peaks in the P 2p spectra of the P-doped RCF alloy/NF at 129.4 (P $2p_{3/2}$) and 130.2 eV (P $2p_{1/2}$) indicated successful P doping and were clearly indexed as M-P bonds that were 0.3 eV lower than the previously reported binding energy of pristine P (red phosphorus) (Fig. 5d) [60]. Therefore, P with relatively high electronegativity acts as an electron acceptor, attracting

electrons from Co and Fe, thus accumulating an electron density cloud at the P sites. As the phosphorization proceeded, the crystal structure of the P-doped RCF alloy/NF changed into a phosphide, as confirmed by XRD analysis (a-RCFP/NF) (Fig. S22). The HRTEM images show that the lattice fringes of 0.188, 0.196, 0.248, and 0.283 nm were assigned to the (211), (112), (111), and (011) planes corresponding to CoP, respectively (PDF #29–0497) (Fig. S23). The RCF alloy/NF maintained its original nanoframe morphology and carbon-encapsulated nanoparticle-based structure, even after phosphorization (Fig. S24). In the Co 2p and Fe 2p XPS spectra, the metallic peaks (Co^0 and Fe^0) of a-RCFP/NF did not shift (Fig. 5a and b). However, in P 2p spectra, the M-P peaks of the a-RCFP/NF showed a positive shift of 0.4 eV, while the Ru^0 peaks in the Ru 3p spectra were negatively shifted by 0.5 eV compared to the P-doped RCF alloy/NF (Fig. 5c and d). In this step, electrons are
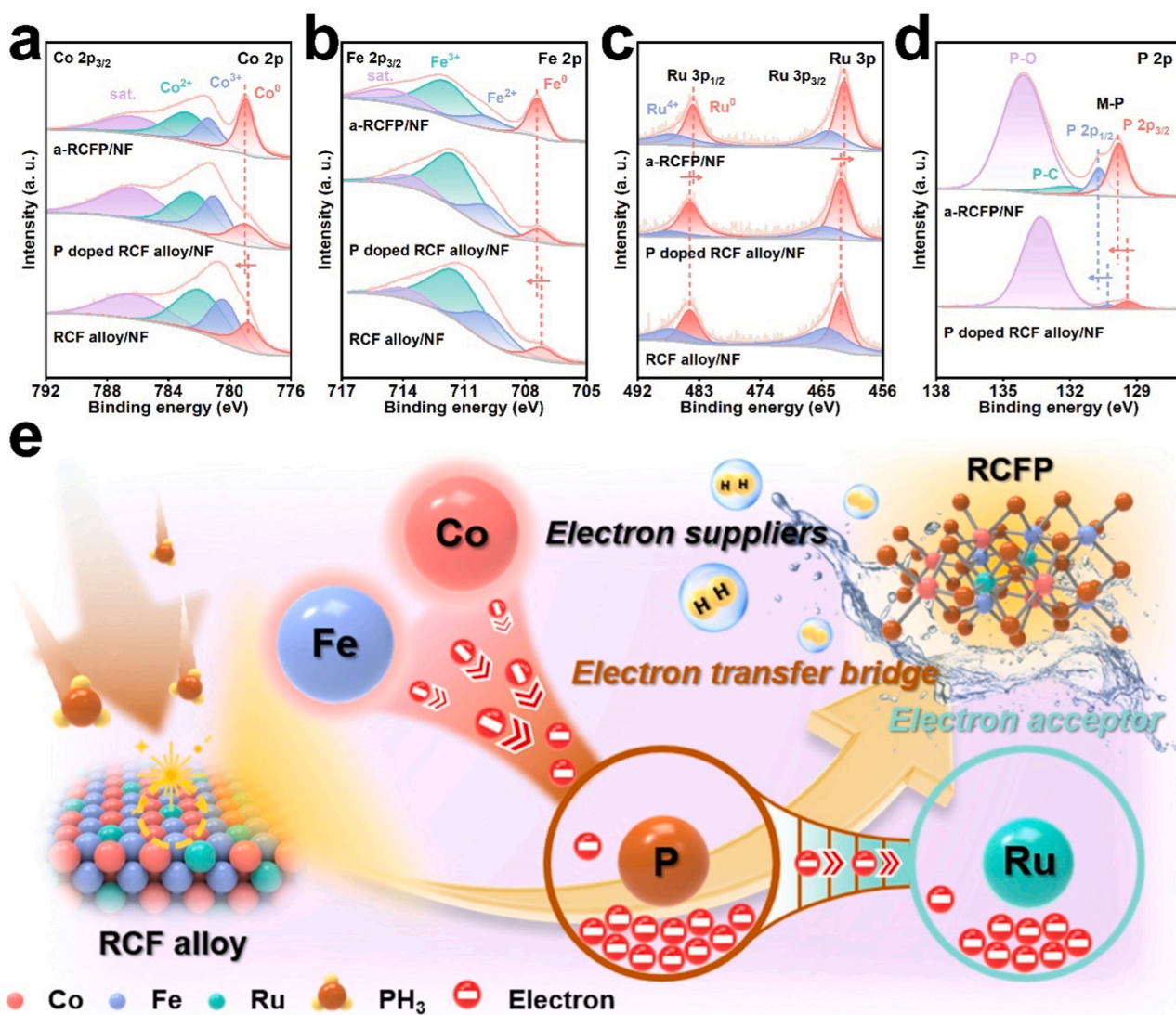
Fig. 5. Electron transfer mechanism in RCFP. XPS (a) Co 2p, (b) Fe 2p, and (c) Ru 3p spectra of a-RCFP/NF, P doped RCF alloy/NF, and RCF alloy/NF. (d) XPS P 2p spectra of a-RCFP/NF and P doped RCF alloy/NF. (e) Schematic for electron transfer pathway during the synthesis of RCFP.

transferred from sufficiently filled P sites serving as electron donors to the Ru sites. Conversely, without the presence of a transition metal (TM) around the Ru-P bond (in the case of pure Ru_xP), the electron density at the P site would not have been fully filled, and the electron transfer from the P site to the Ru site would have been impeded because of their similar electronegativities (Ru: 2.20; P: 2.19) [60–62]. Consequently, it was concluded that the electronic structures of the catalysts were optimized to improve the intrinsic HER activity through synergistic interactions of all the three elements: TMs as electron suppliers, P as an electron transfer bridge, and Ru as an electron acceptor (Fig. 5e) [63, 64].

The RCFP/NF and a-RCFP/NF showed many similarities, such as the same crystalline phase (CoP) and structure encapsulated in carbon; however, several differences were also observed. According to ICP-OES data, the atomic ratio of P to metal in the RCFP/NF and a-RCFP/NF were 1.28 and 1.12, respectively, indicating that a-RCFP/NF contained a relatively lower P content of $\sim$ 13 % (Table. S6). In particular, the intensities of the peaks corresponding to M-P of a-RCFP/NF over all Co 2p, Fe 2p, Ru 3p, and P 2p XPS spectra were relatively lower than those of RCFP/NF, implying the presence of P defects on the surface (Fig. S25) [65]. To further characterize the P defects in the RCFP/NF and a-RCFP/NF, EPR measurements were conducted (Fig. S26). The EPR

signal of a-RCFP/NF, showing a stronger intensity than that of RCFP/NF at a g value of $\sim$ 2.09, demonstrated a higher number of P defects in a-RCFP/NF [66,67]. The carbon layer of the a-RCFP/NF was slightly thicker and more graphitized than that of the RCFP/NF, which might have hindered the inflow of PH_3 gas during the phosphorization process, increasing the number of P defects (Figs. S23 and S27) [68,69].

3.3. Electrocatalytic performance for HER

The HER performances of RCFP/NF, a-RCFP/NF, CFP/NF, and the commercial Pt/C (20 wt %) were measured by LSV in a 1.0 M KOH electrolyte solution using a typical three-electrode system (Fig. 6a). The polarization curve and corresponding Tafel plot for RCFP/NF exhibited a low overpotential of 112 mV at a current density of 10 mA cm^{-2} (η_{10}) with a low Tafel slope of 63.3 mV dec^{-1}, which were much lower than those of CFP/NF (η_{10} = 212 mV with a Tafel slope of 74.7 mV dec^{-1}) and a-RCFP/NF (η_{10} = 142 mV with a Tafel slope of 74.7 mV dec^{-1}) (Fig. 6b and Table. S7). The HER performance changed with Ru content when the Ru content was optimized (Fig. S28 and Table. S1). As the doping amount of Ru increased, the electrocatalytic activity improved to the point where the electronic structure was optimized and then decreased when it exceeded that point (Fig. S29). Therefore, the electronic
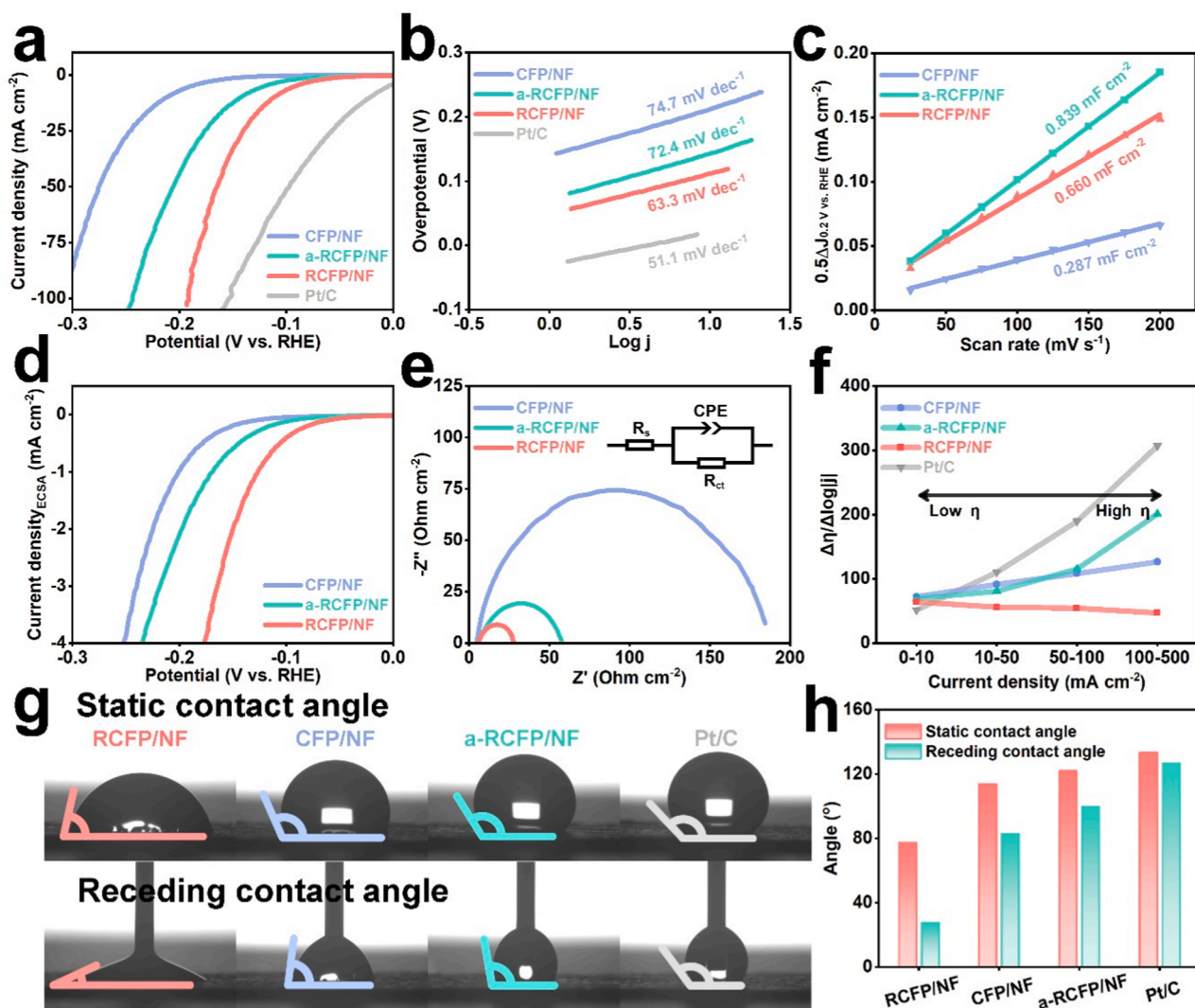
Fig. 6. Electrochemical performances of RCFP/NF. (a) HER polarization curves and (b) Tafel slopes of RCFP/NF, a-RCFP/NF, CFP/NF, and Pt/C. (c) C_{dl}, (d) polarization curves normalized by ECSA, and (e) Nyquist plots of RCFP/NF, a-RCFP/NF, and CFP/NF. (f) Ratios of $\Delta\eta/\Delta\log|j|$ at different current densities of RCFP/NF, a-RCFP/NF, CFP/NF, and Pt/C. Surface property of RCFP/NF. (g) Digital photographs and (h) comparisons for static and receding contact angles of various catalysts.

structure of the catalyst surface was optimized for the HER when the input of the Ru source was 7.5 mg. From the ICP results, the optimal Ru content in the RCFP/NF was 4.7 wt %. (Table. S5).

To better understand the enhanced HER activity of RCFP/NF, ECSA, and EIS were examined. The extrinsic HER performance of the RCFP/NF was improved by adjusting its particle size and morphology. By tuning the particle size, medium-sized RCFP/NF with the largest surface area exhibited the best HER performance (Fig. S30). Moreover, the hollow nanoframe structure of the RCFP/NF provides an advantage for mass transfer and increases the exposure of active sites, resulting in a higher catalytic activity compared to the solid cubic structure (RCFP/NC) (Fig. S31) [23]. The RCFP/NC with relatively small specific surface area and less exposed active sites, showed a higher overpotential of 198 mV at 10 mA cm^{-2} with a Tafel slope of 74.7 mV dec^{-1} (Figs. S31, S32, and S33). Notably, the C_{dl} values of CFP/NF, RCFP/NF, and a-RCFP/NF were evaluated to 0.287, 0.660, and 0.839 mF cm^{-2}, indicating that Ru doping and P defects increased the number of exposed active sites (Figs. 6c and S33). In order to assess the intrinsic characteristics of the electrocatalyst, CFP/NF, RCFP/NF, and a-RCFP/NF were normalized using the ECSA (Fig. 6d). Among them, RCFP/NF exhibited the best intrinsic HER activity, implying that the improved HER catalytic performance was not only due to the enlarged ECSA, but also owing to the optimized intrinsic HER activity derived from the synergistic effects of

Ru doping and phosphorization. To demonstrate the synergistic effect, the polarization curves and Tafel plots of CF alloy/NF, RCF alloy/NF, a-CFP/NF, and a-RCFP/NF were obtained (Fig. S34). RCF alloy/NF showed higher HER activity than CF alloy/NF due to Ru doping, and a-RCFP/NF exhibited better HER performance than RCF alloy/NF attributed to the phosphorization, verifying the synergy effect. Moreover, EIS spectra were evaluated to investigate the interfacial charge transfer (Fig. 6e). In the Nyquist plots, the RCFP/NF exhibited the smallest charge transfer resistance (R_{ct}), indicating that the electronic structure of the RCFP/NF surface optimized via Ru doping and subsequent phosphorization facilitated charge transfer kinetics, which improved the HER kinetics. In order to apply catalysts to a water electrolyzer in practice, it is essential to exhibit excellent electrocatalytic activity on substrates such as carbon paper that are cost-effective and provide good electronic conductivity with a large surface area. The HER performances of RCFP/NF loaded on carbon paper substrate were measured by varying the loading mass (Figs. S35 and S36). When the loading mass reached 1.5 mg cm^{-2}, the RCFP/NF on carbon paper showed low overpotentials of only 45 and 100 mV at current densities of 10 and 100 mA cm^{-2} with a small Tafel slope of 53.0 mV dec^{-1}, which outperformed the recently reported HER catalysts (Table. S7). Furthermore, the electrochemical stability of RCFP/NF on carbon paper was measured by chronopotentiometry at a current density of 100 mA cm^{-2}

and exhibited remarkable stability for more than 100 h (Fig. S37).

Excellent HER performance at high current densities is a key requirement for practical mass hydrogen production [70,71]. RCFP/NF exhibited a very low overpotential of 219 mV at an ultrahigh current density of 500 mA cm^{-2}, thus overwhelming RCFP/NC (η_{500} = 527 mV), CFP/NF (η_{500} = 390 mV), a-RCFP/NF (η_{500} = 378 mV), and even commercial Pt/C (η_{500} = 364 mV) (Fig. S38). The relationships between $\Delta\eta/\Delta\log|j|$ ratio and current density $|j|$ were investigated to ensure the high current density HER performance (Fig. 6f and S39). The fast mass transfer capability and excellent intrinsic activity, especially in large current density regions, are critical variables in boosting HER performance. A catalyst with a smaller $\Delta\eta/\Delta\log|j|$ ratio has a faster mass transfer capability [70,72,73]. Even at 100–500 mA cm^{-2}, the $\Delta\eta/\Delta\log|j|$ ratio of RCFP/NF remained small, manifesting the superior mass transfer capability at high current densities. However, the $\Delta\eta/\Delta\log|j|$ ratio of the other catalysts increased rapidly due to their poor mass transfer capability at high current densities (Table. S8). The static and receding contact angles were measured to evaluate the hydrophilicity and aerophobicity associated with the mass transfer of the catalysts. The

static contact angle of RCFP/NF was 77°, which is much smaller than those of CFP/NF (114°), a-RCFP/NF (122°), RCFP/NC (128°), and Pt/C (134°), indicating that it is more hydrophilic (Fig. 6g, h, and S40). The high hydrophilicity improves the electrolyte affinity to the surface of a catalyst, which then facilitates contact between the active sites and electrolyte, thereby accelerating mass transfer kinetics, especially in the HER Volmer step [74,75]. Furthermore, the dynamic sessile drop method was used to estimate the aerophobic properties of the catalysts by measuring the receding contact angles. If the evolved H$_2$ does not detach rapidly during the HER, the H$_2$ bubbles agglomerate on the catalyst surface and cover the active sites, reducing the reaction area of the catalyst. Typically, on an aerophobic electrocatalyst surface with a small receding contact angle, bubbles easily detach from the surface before growing [76,77]. A minimum receding contact angle of 28° was observed for RCFP/NF compared to those of CFP/NF (83°), a-RCFP/NF (100°), RCFP/NC (115°), and Pt/C (127°). This superaerophobic characteristic of the RCFP/NF promoted its mass-transfer capability by facilitating the removal of H$_2$ bubbles from the surface. Overall, the RCFP/NF adjusted the electronic structure into a unique hollow
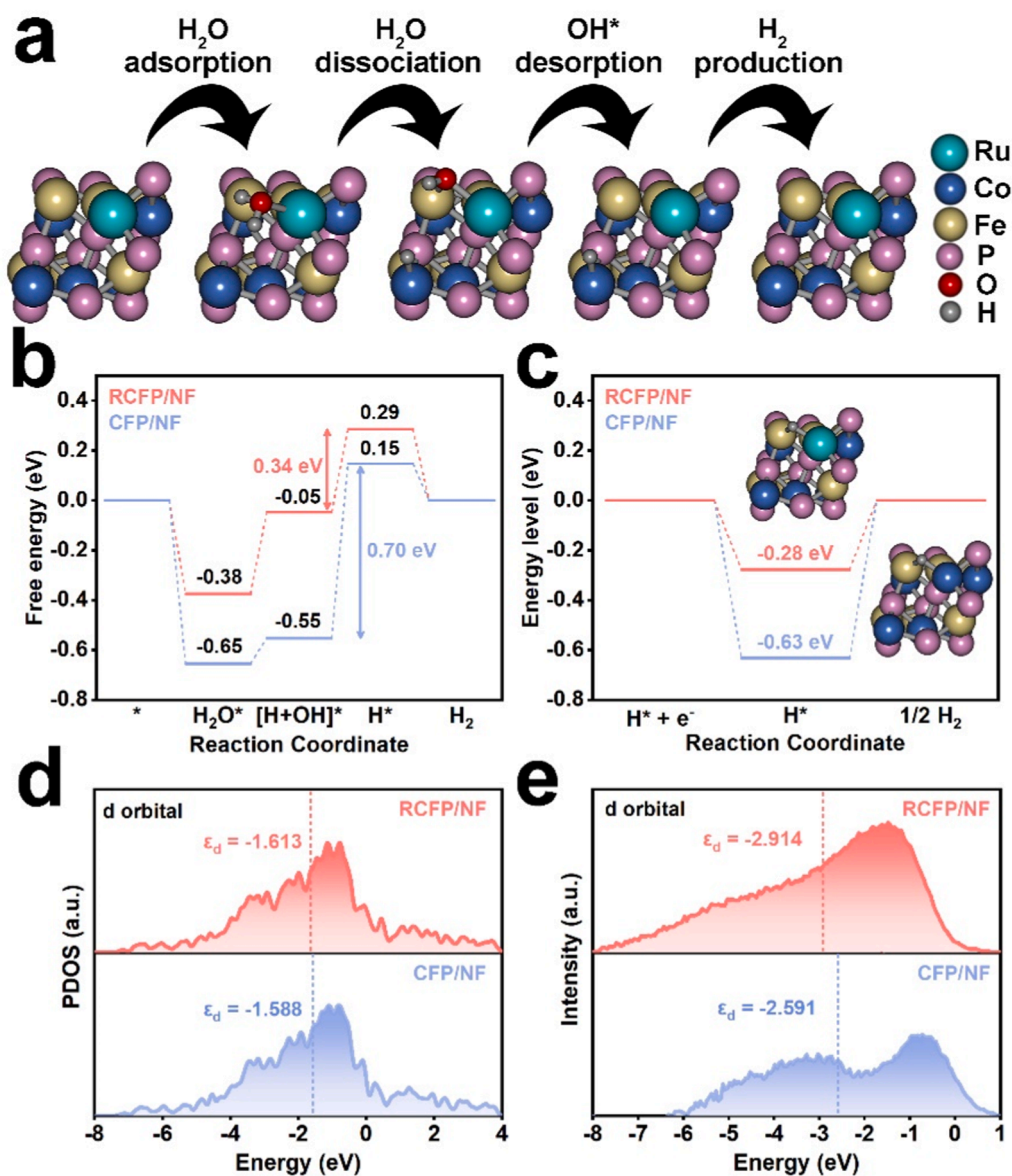

Fig. 7. Theoretical calculations. (a) Four elementary steps of the alkaline HER pathways and (b) corresponding free energy diagram on RCFP (111) slab. (c) Free energy diagram of H* adsorption for the Ru-Fe and Co-Fe bridge sites. (d) Calculated PDOS of D-orbitals and (e) measured surface valence band photoemission spectra of RCFP/NF and CFP/NF.

nanoframe structure exhibiting superior hydrophilic and aerophobic characteristics, resulting in a superior HER performance, especially at a high current density.

DFT calculations were performed to investigate the intrinsic contributions of the modulated electronic structures of the RCFP/NF to improve the HER performance under alkaline conditions. Generally, in an alkaline medium, the HER occurs in two steps: First, water molecules are adsorbed on the surface of the catalyst and dissociate (Volmer step: * + H_2O + e$^-$ → H* + OH$^-$). Second, water dissociation (Heyrovsky step: H* + H_2O + e$^-$ → H_2 + OH$^-$) or chemical combination of two adsorbed H atoms (Tafel step: H* + H* → H_2) occurs [78,79]. As shown in the Tafel plots, the Tafel slopes of RCFP/NF (63.3 mV dec^{-1}) and CFP/NF (74.7 mV dec^{-1}) indicated that our samples followed the Volmer–Heyrovsky mechanism; thus, we established a computational model mainly based on that pathway (Figs. 6b and 7a) [80]. According to the free energy diagram, CFP/NF displayed a large energy barrier of 0.70 eV for OH* desorption (Fig. 7b). In contrast, RCFP/NF exhibited a much smaller energy barrier (0.34 eV for OH* desorption, indicating that Ru doping successfully facilitated the Volmer reaction kinetics in the alkaline HER. In addition, the Ru-Fe at the bridge site, which is another hydrogen adsorption site candidate for RCFP/NF, exhibited a Gibbs free energy value of adsorbed H (ΔG_{H*} = −0.28 eV), which is much closer to zero than that of Co-Fe for CFP/NF (ΔG_{H*} = −0.63 eV). This weakened the adsorption strength for evolved H_2 (Fig. 7c). Further

studies on the D-band center (ε_d) were conducted to determine the effect of the tailored electronic structure and binding strength of the adsorbate (OH*/H*) (Fig. 7d). According to the D-band theory, the closer the ε_d position to the Fermi level, the stronger the binding between catalyst surface and adsorbates due to the rise of antibonding states [81–83]. Based on the projected density of states (PDOS) of the D-orbitals, the ε_d value of RCFP/NF (ε_d = −1.613) was lower than that of CFP/NF (ε_d = −1.588). Ru heteroatom doping modified the electronic structure, thereby significantly shifting the ε_d away from the Fermi level, which successfully weakened the excessive interaction between the adsorbates (OH*/H*) and RCFP/NF. Additionally, the surface valence band spectra of the RCFP/NF and CFP/NF were collected using high-resolution XPS to support the above computational calculations (Fig. 7e) [84]. Ru insertion contributed to the downward shift of the D-band center, which showed the same trend as that observed in the PDOS calculation. In summary, both the theoretical and experimental results confirmed that the outstanding HER activity of RCFP/NF originated from the pronounced OH* desorption and moderate H* adsorption energy. In particular, the excellent OH* desorption ability, which facilitates the sluggish kinetics of the Volmer reaction, strongly affects the HER performance particularly at high current densities, as confirmed by electrochemical measurements (Fig. 6f and S38) [85].

Long-term stability is a vital indicator of the electrocatalytic performance. The stabilities of the RCFP/NF and commercial Pt/C were
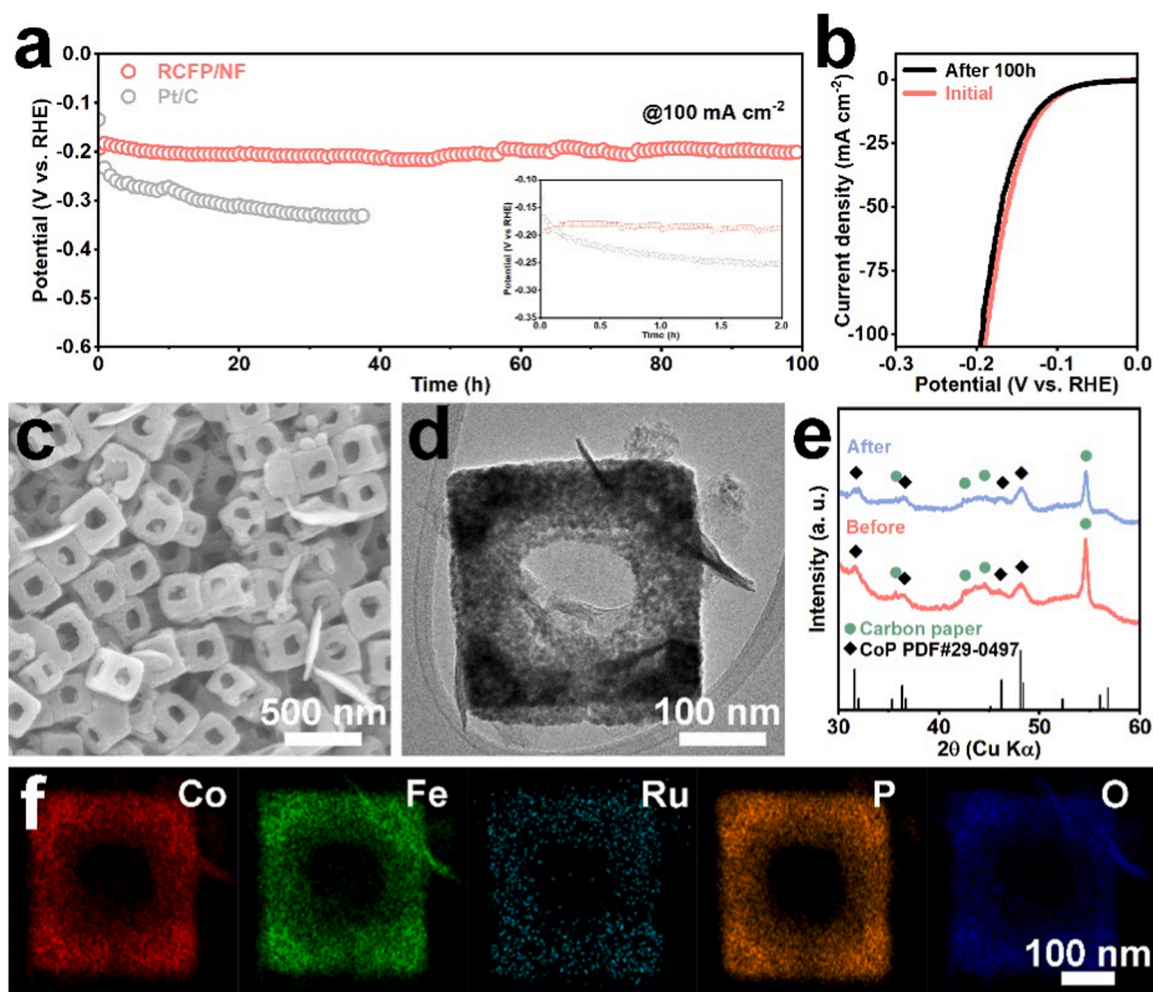

Fig. 8. Stability test of RCFP/NF. (a) Chronopotentiometric tests of RCFP/NF and Pt/C in 1.0 M KOH at a current density of 100 mA cm^{-2} (Inset image: chronopotentiometric tests for the initial 2 h). (b) HER polarization curves of the RCFP/NF before and after 100 h of the stability test. (c) SEM and (d) TEM images after the stability test. (e) XRD patterns of RCFP/NF loaded onto carbon paper before and after 100 h of the stability test. (f) EDS mapping of RCFP/NF after 100 h of the stability test.

evaluated by chronopotentiometry at a current density of 100 mA cm^{-2} (Fig. 8a). The operating potential of the RCFP/NF exhibited negligible change even after 100 h, indicating outstanding long-term stability in alkaline HER condition, whereas Pt/C showed severe degradation after only 30 h. Even after the 100 h of the chronopotentiometry test, the polarization curve showed little shift compared to the initial curve (Fig. 8b). In order to quantify the generated hydrogen gas and verify the Faradaic efficiency of RCFP/NF for HER, the same chronopotentiometry test at 100 mA cm^{-2} was performed with the GC measurement (Fig. S41) [86]. The amount of produced hydrogen gas was identical to the theoretically calculated amount of hydrogen, and the hydrogen evolution rate of 5.18 μmol cm^{-2} s^{-1} remained over time. The RCFP/NF catalyst exhibited near 100 % Faradaic efficiency, indicating that all charges were consumed for stable HER.

To further investigate the microstructural changes in the catalyst during the long-term stability tests, SEM and TEM images were obtained after chronopotentiometry (Fig. 8c, d, and S42). The RCFP/NF showed a negligible change in its original nanoframe structure, but a small amount of nanosheet structure was formed during the HER. The post-HER RCFP/NF was characterized to verify the nanosheets generated after the long-term stability tests. No new diffraction peaks were detected in the ex situ XRD pattern owing to low loading and low crystallinity (Fig. 8e). The TEM-EDS elemental mapping data suggests that the RCFP/NF was partially oxidized and deformed into a sheet structure without the dissolution of metals (Fig. 8f and S43) [22]. The reduced intensity of the P 2p XPS spectrum and ICP-MS results demonstrate that P dissolved in the alkaline electrolyte during the HER, which led to the exposure of the metal active sites on the surface, thereby forming in situ metal oxides/hydroxides (Fig. S44 and Table. S9) [54]. In addition, the Co 2p, Fe 2p, and Ru 3p spectra revealed that all the peak intensities corresponding to M-O increased as M-P decreased after the stability test, confirming that the metal phosphide was partially transformed into metal oxides/hydroxides [87]. Additionally, the binding energy shifts of the M-P peaks in the Co 2p, Fe 2p, Ru 3p, and P 2p spectra were observed to be less than 0.1 eV, and only small amounts of dissolved metals were detected by ICP-MS, indicating the excellent electrochemical stability of RCFP/NF in alkaline electrolytes. This robustness of the RCFP/NF can be attributed to the carbon layer encapsulating the nanoparticles preventing the dissolution of metal atoms and structural deformation [88,89].

4. Conclusions

In this study, a Ru-doped CoFeP 3D nanoframe encapsulated in an N, P co-doped carbon layer was successfully synthesized as a potential HER electrocatalyst in alkaline media. By adjusting the Ru content and size of the nanoframe structure, RCFP/NF exhibited an outstanding HER performance at high current densities and an extraordinarily low overpotential of 219 mV at 500 mA cm^{-2}. XPS analyses rationalized the electron transfer pathways during Ru doping and subsequent phosphorization processes. Ru with a high electronegativity can effectively modulate the electronic structure of CFP and induce a downshift of the D-band center, resulting in an optimized electronic structure with optimized OH*/H* adsorption energy. Moreover, RCFP/NF have the advantage of accelerating the mass transfer kinetics owing to their high hydrophilicity and low aerophobicity, mainly derived from Ru doping and its open hollow nanoframe structure, which are key factors for the HER at high current densities.

CRediT authorship contribution statement

Kunik Jang: Methodology, Investigation, Data curation, Visualization, Writing - Original Draft. **Hyunseok Yoon:** Methodology, Investigation, Validation. **Ji Seong Hyoung:** Data curation, Visualization. **Dwi Sakti Aldianto Pratama:** DFT calculations. **Chan Woo Lee:** Validation, Supervision. **Dong-Wan Kim:** Conceptualization, Supervision, Project administration, Writing - Review & Editing.

Declaration of Competing Interest

The authors declare that they have no known competing financial interests or personal relationships that could have appeared to influence the work reported in this paper.

Data Availability

Data will be made available on request.

Appendix A. Supporting information

Supplementary data associated with this article can be found in the online version at doi:10.1016/j.apcatb.2023.123327.

References

[1] Y. Wu, X. Liu, D. Han, X. Song, L. Shi, Y. Song, S. Niu, Y. Xie, J. Cai, S. Wu, J. Kang, J. Zhou, Z. Chen, X. Zheng, X. Xiao, G. Wang, Electron density modulation of NiCo$_2$S$_4$ nanowires by nitrogen incorporation for highly efficient hydrogen evolution catalysis, Nat. Commun. 9 (2018), 1425, https://doi.org/10.1038/s41467-018-03858-w.

[2] N. Mahmood, Y. Yao, J.W. Zhang, L. Pan, X. Zhang, J.J. Zou, Electrocatalysts for hydrogen evolution in alkaline electrolytes: Mechanisms, challenges, and prospective solutions, Adv. Sci. 5 (2018), 1700464, https://doi.org/10.1002/advs.201700464.

[3] C. Liu, C. Kong, F.-J. Zhang, C.-M. Kai, W.-Q. Cai, X.-Y. Sun, W.-C. Oh, Research progress of defective MoS$_2$ for photocatalytic hydrogen evolution, J. Korean Ceram. Soc. 58 (2021) 135–147, https://doi.org/10.1007/s43207-020-00103-3.

[4] B.A. Yusuf, C. Xia, M. Xie, W. Yaseen, J. Xie, Y. Xu, Scalable fabrication of Ru-Mo$_2$C composite catalytic material with carbon-based core–shell structure and its remarkable application for hydrogen evolution reaction, J. Electroanal. Chem. 921 (2022), 116643, https://doi.org/10.1016/j.jelechem.2022.116643.

[5] B.A. Yusuf, W. Yaseen, J. Xie, A.A. Babangida, A.I. Muhammad, M. Xie, Y. Xu, Rational design of noble metal-based multimetallic nanomaterials: a review, Nano Energy (2022), 107959, https://doi.org/10.1016/j.nanoen.2022.107959.

[6] F. Yu, H.Q. Zhou, Y.F. Huang, J.Y. Sun, F. Qin, J.M. Bao, W.A. Goddardiii, S. Chen, Z.F. Ren, High-performance bifunctional porous non-noble metal phosphide catalyst for overall water splitting, Nat. Commun. 9 (2018), 2551, https://doi.org/10.1038/s41467-018-04746-z.

[7] X.K. Huang, X.P. Xu, C. Li, D.F. Wu, D.J. Cheng, D.P. Cao, Vertical CoP nanoarray wrapped by N,P-doped carbon for hydrogen evolution reaction in both acidic and alkaline conditions, Adv. Energy Mater. 9 (2019), 1803970, https://doi.org/10.1002/aenm.201803970.

[8] G.W. Li, Y. Sun, J.C. Rao, J.Q. Wu, A. Kumar, Q.N. Xu, C.G. Fu, E.K. Liu, G.R. Blake, P. Werner, B.Q. Shao, K. Liu, S. Parkin, X.J. Liu, M. Fahlman, S.C. Liou, G. Auffermann, J. Zhang, C. Felser, X.L. Feng, Carbon-tailored semimetal mop as an efficient hydrogen evolution electrocatalyst in both alkaline and acid media, Adv. Energy Mater. 8 (2018), 1801258, https://doi.org/10.1002/aenm.201801258.

[9] J.H. Chen, J.W. Liu, J.Q. Xie, H.Q. Ye, X.Z. Fu, R. Sun, C.P. Wong, Co-Fe-P nanotubes electrocatalysts derived from metal-organic frameworks for efficient hydrogen evolution reaction under wide pH range, Nano Energy 56 (2019) 225–233, https://doi.org/10.1016/j.nanoen.2018.11.051.

[10] X.K. Huang, L. Gong, H. Xu, J.H. Qin, P. Ma, M. Yang, K.Z. Wang, L. Ma, X. Mu, R. Li, Hierarchical iron-doped CoP heterostructures self-assembled on copper foam as a bifunctional electrocatalyst for efficient overall water splitting, J. Colloid Interface Sci. 569 (2020) 140–149, https://doi.org/10.1016/j.jcis.2020.02.073.

[11] D. Liu, G. Xu, H. Yang, H. Wang, B.Y. Xia, Rational design of transition metal phosphide-based electrocatalysts for hydrogen evolution, Adv. Energy Mater. 33 (2023), 2208358, https://doi.org/10.1002/adfm.202208358.

[12] X. Yang, Y. Liu, R. Guo, J. Xiao, Ru doping boosts electrocatalytic water splitting, Dalton Trans. 51 (2022) 11208–11225, https://doi.org/10.1039/d2dt01394k.

[13] Q. Yao, B. Huang, N. Zhang, M. Sun, Q. Shao, X. Huang, Channel-rich RuCu nanosheets for pH-universal overall water splitting electrocatalysis, Angew. Chem. Int. Ed. 131 (2019) 14121–14126, https://doi.org/10.1002/ange.201908092.

[14] P. Zhai, M. Xia, Y. Wu, G. Zhang, J. Gao, B. Zhang, S. Cao, Y. Zhang, Z. Li, Z. Fan, C. Wang, X. Zhang, J.T. Miller, L. Sun, J. Hou, Engineering single-atomic ruthenium catalytic sites on defective nickel-iron layered double hydroxide for overall water splitting, Nat. Commun. 12 (2021), 4587, https://doi.org/10.1038/s41467-021-24828-9.

[15] M.J. Qu, Y.M. Jiang, M. Yang, S. Liu, Q.F. Guo, W. Shen, M. Li, R.X. He, Regulating electron density of NiFe-P nanosheets electrocatalysts by a trifle of ru for high-efficient overall water splitting, Appl. Catal. B: Environ. 263 (2020), 118324, https://doi.org/10.1016/j.apcatb.2019.118324.

[16] C. Wang, L.M. Qi, Heterostructured inter-doped ruthenium-cobalt oxide hollow nanosheet arrays for highly efficient overall water splitting, Angew. Chem. Int. Ed. 59 (2020) 17219–17224, https://doi.org/10.1002/anie.202005436.

[17] J. Su, Y. Yang, G. Xia, J. Chen, P. Jiang, Q. Chen, Ruthenium-cobalt nanoalloys encapsulated in nitrogen-doped graphene as active electrocatalysts for producing hydrogen in alkaline media, Nat. Commun. 8 (2017), 14969, https://doi.org/10.1038/ncomms14969.

[18] B. Lu, C. Lv, Y. Xie, L. Gao, J. Yan, K. Zhu, G. Wang, D. Cao, K. Ye, Exploring the synergistic effect of CoSeP/CoP interface catalyst for efficient urea electrolysis, Small (2023), 2302923, https://doi.org/10.1002/smll.202302923.

[19] S.J. You, X.B. Gong, W. Wang, D.P. Qi, X.H. Wang, X.D. Chen, N.Q. Ren, Enhanced cathodic oxygen reduction and power production of microbial fuel cell based on noble-metal-free electrocatalyst derived from metal-organic frameworks, Adv. Energy Mater. 6 (2016), 1501497, https://doi.org/10.1002/aenm.201501497.

[20] W.X. Li, B. Yu, Y. Hu, X.Q. Wang, B. Wang, X.J. Zhang, D.X. Yang, Z.G. Wang, Y. F. Chen, Encapsulating hollow (Co,Fe)P nanoframes into N,P-codoped graphene aerogel for highly efficient water splitting, J. Power Sources 456 (2020), 228015, https://doi.org/10.1016/j.jpowsour.2020.228015.

[21] D.M. Liu, H. Xu, C. Wang, C.Q. Ye, R. Yu, Y.K. Du, In situ etch engineering of Ru doped NiFe(OH)$_x$/NiFe-MOF nanocomposites for boosting the oxygen evolution reaction, J. Mater. Chem. A 9 (2021) 24670–24676, https://doi.org/10.1039/d1ta06438j.

[22] Y. Lian, H. Sun, X. Wang, P. Qi, Q. Mu, Y. Chen, J. Ye, X. Zhao, Z. Deng, Y. Peng, Carved nanoframes of cobalt-iron bimetal phosphide as a bifunctional electrocatalyst for efficient overall water splitting, Chem. Sci. 10 (2019) 464–474, https://doi.org/10.1039/c8sc03877e.

[23] L. Ji, J. Wang, X. Teng, T.J. Meyer, Z. Chen, CoP nanoframes as bifunctional electrocatalysts for efficient overall water splitting, ACS Catal. 10 (2019) 412–419, https://doi.org/10.1021/acscatal.9b03623.

[24] C.C. McCrory, S. Jung, I.M. Ferrer, S.M. Chatman, J.C. Peters, T.F. Jaramillo, Benchmarking hydrogen evolving reaction and oxygen evolving reaction electrocatalysts for solar water splitting devices, J. Am. Chem. Soc. 137 (2015) 4347–4357, https://doi.org/10.1021/ja510442p.

[25] S.K. Bikkarolla, P. Papakonstantinou, CuCo$_2$O$_4$ nanoparticles on nitrogenated graphene as highly efficient oxygen evolution catalyst, J. Power Sources 281 (2015) 243–251, https://doi.org/10.1016/j.jpowsour.2015.01.192.

[26] T.T. Li, J.J. Qian, Y.Q. Zheng, Facile synthesis of porous CuO polyhedron from Cu-based metal organic framework (MOF-199) for electrocatalytic water oxidation, RSC Adv. 6 (2016) 77358–77365, https://doi.org/10.1039/c6ra18781a.

[27] P. Giannozzi, S. Baroni, N. Bonini, M. Calandra, R. Car, C. Cavazzoni, D. Ceresoli, Quantum espresso: a modular and open-source software project for quantum simulations of materials, J. Phys. Condens. Matter 21 (2009), 395502.

[28] P. Giannozzi, J. Phys.: Condens Matt 29 (2017), 465901.

[29] M.S. Virtual Lab. Inc., ⟨https://www.Materialssquare.com/⟩ 2017.

[30] M. Ernzerhof, J.P. Perdew, Generalized gradient approximation to the angle- and system-averaged exchange hole, J. Chem. Phys. 109 (1998) 3313–3320, https://doi.org/10.1063/1.476928.

[31] J.K. Nørskov, T. Bligaard, A. Logadottir, J. Kitchin, J.G. Chen, S. Pandelov, U. Stimming, Trends in the exchange current for hydrogen evolution, J. Electrochem. Soc. 152 (2005) J23.

[32] J. Nai, B.Y. Guan, L. Yu, X.W.D. Lou, Oriented assembly of anisotropic nanoparticles into frame-like superstructures, Sci. Adv. 3 (2017), e1700732, https://doi.org/10.1126/sciadv.1700732.

[33] W. Lu, H. Lee, J. Cha, J. Zhang, I. Chung, Electronic structure manipulation of the mott insulator RuCl$_3$ via single-crystal to single-crystal topotactic transformation, Angew. Chem. Int. Ed. 62 (2023), e202219344, https://doi.org/10.1002/anie.202219344.

[34] Y. Yan, J. Huang, X. Wang, T. Gao, Y. Zhang, T. Yao, B. Song, Ruthenium incorporated cobalt phosphide nanocubes derived from a prussian blue analog for enhanced hydrogen evolution, Front. Chem. 6 (2018), 521, https://doi.org/10.3389/fchem.2018.00521.

[35] A.S. Kumar, P.Y. Chen, S.H. Chien, J.M. Zen, Development of an enzymeless/mediatorless glucose sensor using ruthenium oxide-prussian blue combinative analogue, Electroanalysis 17 (2005) 210–222, https://doi.org/10.1002/elan.200403086.

[36] J. Kim, S.H. Yi, L. Li, T.V. Thu, S.E. Chun, Effect of valence state of cobalt in cobalt hexacyanoferrate coprecipitated at different temperatures on electrochemical behavior, Int. J. Energy Res. 46 (2022) 22717–22729, https://doi.org/10.1002/er.8574.

[37] Y.Q. Feng, X. Wang, P.P. Dong, J. Li, L. Feng, J.F. Huang, L.Y. Cao, L.L. Feng, K. Kajiyoshi, C.R. Wang, Boosting the activity of prussian-blue analogue as efficient electrocatalyst for water and urea oxidation, Sci. Rep. 9 (2019), 15965, https://doi.org/10.1038/s41598-019-52412-1.

[38] P.J. Kulesza, M.A. Malik, A. Denca, J. Strojek, In situ ft-ir/atr spectroelectrochemistry of prussian blue in the solid state, Anal. Chem. 68 (1996) 2442–2446, https://doi.org/10.1021/ac950380k.

[39] Y. Feng, P. Dong, L. Cao, X. Wang, J. Wang, H. Wang, W. Feng, J. Chen, L. Feng, C. He, J. Huang, Defect-rich bimetallic yolk–shell metal-cyanide frameworks as efficient electrocatalysts for oxygen evolution reactions, J. Mater. Chem. A 9 (2021) 2135–2144, https://doi.org/10.1039/d0ta09892b.

[40] J.H. Lee, J.G. Bae, H.J. Lee, J.H. Lee, Unveiling anomalous lattice shrinkage induced by pi-backbonding in prussian blue analogues, J. Energy Chem. 70 (2022) 121–128, https://doi.org/10.1016/j.jechem.2022.02.032.

[41] X. Wei, J. Wei, Y. Song, D. Wu, X.D. Liu, H. Chen, P. Xiao, Y. Zhang, Potassium mediated Co–Fe-based prussian blue analogue architectures for aqueous potassium-ion storage, Chem. Commun. 57 (2021) 7019–7022.

[42] Y. Wang, Y. Du, Z. Fu, J. Ren, Y. Fu, L. Wang, Construction of Ru/FeCoP heterointerface to drive dual active site mechanism for efficient overall water splitting, J. Mater. Chem. A 10 (2022) 16071–16079, https://doi.org/10.1039/d2ta03465d.

[43] C. Wang, L. Qi, Hollow nanosheet arrays assembled by ultrafine Ruthenium–Cobalt phosphide nanocrystals for exceptional pH-universal hydrogen evolution, ACS Mater. Lett. 3 (2021) 1695–1701, https://doi.org/10.1021/acsmaterialslett.1c00532.

[44] K. Ye, T. Liu, Y. Song, Q. Wang, G. Wang, Tailoring the interactions of heterogeneous Ag$_2$S/Ag interface for efficient CO$_2$ electroreduction, Appl. Catal. B: Environ. 296 (2021), 120342, https://doi.org/10.1016/j.apcatb.2021.120342.

[45] Q.H. Yang, Z.H. Li, R.K. Zhang, L. Zhou, M.F. Shao, M. Wei, Carbon modified transition metal oxides/hydroxides nanoarrays toward high-performance flexible all-solid-state supercapacitors, Nano Energy 41 (2017) 408–416, https://doi.org/10.1016/j.nanoen.2017.09.049.

[46] X.X. Yan, M.Y. Gu, Y. Wang, L. Xu, Y.W. Tang, R.B. Wu, In-situ growth of Ni nanoparticle-encapsulated N-doped carbon nanotubes on carbon nanorods for efficient hydrogen evolution electrocatalysis, Nano Res. 13 (2020) 975–982, https://doi.org/10.1007/s12274-020-2727-7.

[47] H. Jia, N. Shang, J. Chen, Q. Yang, M. Su, M. Li, Y. Zhang, Facile synthesis of N-doped carbon nanoframes encapsulated by CoP nanoparticles for hydrogen evolution reaction, J. Colloid Interface Sci. 601 (2021) 338–345, https://doi.org/10.1016/j.jcis.2021.05.139.

[48] F. Yang, X. Chen, Z. Li, D.F. Wang, L.Q. Liu, J.H. Ye, Ultrathin FeP nanosheets as an efficient catalyst for electrocatalytic water oxidation: Promoted intermediates adsorption by surface defects, ACS Appl. Energy Mater. 3 (2020) 3577–3585, https://doi.org/10.1021/acsaem.0c00080.

[49] A.P. Grosvenor, S.D. Wik, R.G. Cavell, A. Mar, Examination of the bonding in binary transition-metal monophosphides MP (M = Cr, Mn, Fe, Co) by x-ray photoelectron spectroscopy, Inorg. Chem. 44 (2005) 8988–8998, https://doi.org/10.1021/ic051004d.

[50] J. Huang, P. Xu, T. Gao, J. Huangfu, X.-j Wang, S. Liu, Y. Zhang, B. Song, Controlled synthesis of hollow bimetallic prussian blue analog for conversion into efficient oxygen evolution electrocatalyst, ACS Sustain. Chem. Eng. 8 (2019) 1319–1328, https://doi.org/10.1021/acssuschemeng.9b07122.

[51] P. Li, W. Li, S. Zhao, Y. Huang, S. Tian, X. Huang, Advanced hydrogen evolution electrocatalysis enabled by ruthenium phosphide with tailored hydrogen binding strength via interfacial electronic interaction, Chem. Eng. J. 429 (2022), 132557, https://doi.org/10.1016/j.cej.2021.132557.

[52] J.B. Zhu, S. Li, M.L. Xiao, X. Zhao, G.R. Li, Z.Y. Bai, M. Li, Y.F. Hu, R.F. Feng, W. W. Liu, R. Gao, D. Su, A.P. Yu, Z.W. Chen, Tensile-strained ruthenium phosphide by anion substitution for highly active and durable hydrogen evolution, Nano Energy 77 (2020), 105212, https://doi.org/10.1016/j.nanoen.2020.105212.

[53] J. Yu, Y.N. Guo, S.X. She, S.S. Miao, M. Ni, W. Zhou, M.L. Liu, Z.P. Shao, Bigger is surprisingly better: Agglomerates of larger RuP nanoparticles outperform benchmark Pt nanocatalysts for the hydrogen evolution reaction, Adv. Mater. 30 (2018), 1800047, https://doi.org/10.1002/adma.201800047.

[54] Y.Y. Song, J.L. Cheng, J. Liu, Q. Ye, X. Gao, J.J. Lu, Y.L. Cheng, Modulating electronic structure of cobalt phosphide porous nanofiber by ruthenium and nickel dual doping for highly-efficiency overall water splitting at high current density, Appl. Catal. B: Environ. 298 (2021), 120488, https://doi.org/10.1016/j.apcatb.2021.120488.

[55] P.F. Guo, R.B. Wu, B. Fei, J. Liu, D. Liu, X.X. Yan, H.G. Pan, Multifunctional bayberry-like composites consisting of CoFe encapsulated by carbon nanotubes for overall water splitting and zinc-air batteries, J. Mater. Chem. A 9 (2021) 21741–21749, https://doi.org/10.1039/d1ta06100c.

[56] F.F. Zhang, Y.L. Zhu, Y. Chen, Y.Z.H. Lu, Q. Lin, L. Zhang, S.W. Tao, X.W. Zhang, H. T. Wang, RuCo alloy bimodal nanoparticles embedded in N-doped carbon: A superior pH-universal electrocatalyst outperforms benchmark Pt for the hydrogen evolution reaction, J. Mater. Chem. A 8 (2020) 12810–12820, https://doi.org/10.1039/d0ta04491a.

[57] C.Y. Su, H. Cheng, W. Li, Z.Q. Liu, N. Li, Z.F. Hou, F.Q. Bai, H.X. Zhang, T.Y. Ma, Atomic modulation of FeCo-nitrogen-carbon bifunctional oxygen electrodes for rechargeable and flexible all-solid-state zinc-air battery, Adv. Energy Mater. 7 (2017), 1602420, https://doi.org/10.1002/aenm.201602420.

[58] S. Iqbal, S.A. Kondrat, D.R. Jones, D.C. Schoenmakers, J.K. Edwards, L. Lu, B. R. Yeo, P.P. Wells, E.K. Gibson, D.J. Morgan, C.J. Kiely, G.J. Hutchings, Ruthenium nanoparticles supported on carbon: an active catalyst for the hydrogenation of lactic acid to 1,2-propanediol, ACS Catal. 5 (2015) 5047–5059, https://doi.org/10.1021/acscatal.5b00625.

[59] Q.J. Zhi, S.B. Qin, W.P. Liu, R. Jiang, T.T. Sun, K. Wang, P. Jin, J.Z. Jiang, Ultralow loading of ruthenium nanoparticles on nitrogen-doped porous carbon enables ultrahigh mass activity for the hydrogen evolution reaction in alkaline media, Catal. Sci. Technol. 11 (2021) 3182–3188, https://doi.org/10.1039/d1cy00364j.

[60] X.H. Wu, K.L. Gong, G.Q. Zhao, W.J. Lou, X.B. Wang, W.M. Liu, Mechanical synthesis of chemically bonded phosphorus-graphene hybrid as high-temperature lubricating oil additive, RSC Adv. 8 (2018) 4595–4603, https://doi.org/10.1039/c7ra11691h.

[61] Y.M. Zhao, X.W. Wang, G.Z. Cheng, W. Luo, Phosphorus-induced activation of ruthenium for boosting hydrogen oxidation and evolution electrocatalysis, ACS Catal. 10 (2020) 11751–11757, https://doi.org/10.1021/acscatal.0c03148.

[62] Y. Wang, Z. Liu, H. Liu, N.T. Suen, X. Yu, L.G. Feng, Electrochemical hydrogen evolution reaction efficiently catalyzed by Ru_2P nanoparticles, Chemsuschem 11 (2018) 2724–2729, https://doi.org/10.1002/cssc.201801103.

[63] F. Xue, Y.T. Si, C. Cheng, W.L. Fu, X.Y. Chen, S.H. Shen, L.Z. Wang, M.C. Liu, Electron transfer via homogeneous phosphorus bridges enabling boosted photocatalytic generation of H_2 and H_2O_2 from pure water with stoichiometric ratio, Nano Energy 103 (2022), 107799, https://doi.org/10.1016/j.nanoen.2022.107799.

[64] R.N. Zhan, Y.F. Zhou, C. Liu, X.J. Wang, X.L. Sun, Y.Q. Zhu, J.F. Niu, Insights into mechanism of Fe-dominated active sites via phosphorus bridging in Fe-Ni bimetal single atom catalysts, Sep. Purif. Technol. 286 (2022) 120443, https://doi.org/10.1016/j.seppur.2022.120443.

[65] Y.T. Yan, J.H. Lin, J. Cao, S. Guo, X.H. Zheng, J.C. Feng, J.L. Qi, Activating and optimizing the activity of NiCoP nanosheets for electrocatalytic alkaline water splitting through the V doping effect enhanced by P vacancies, J. Mater. Chem. A 7 (2019) 24486–24492, https://doi.org/10.1039/c9ta09283h.

[66] X.C. Zhou, H. Gao, Y.F. Wang, Z. Liu, J.Q. Lin, Y. Ding, P vacancies-enriched 3D hierarchical reduced cobalt phosphide as a precursor template for defect engineering for efficient water oxidation, J. Mater. Chem. A 6 (2018) 14939–14948, https://doi.org/10.1039/c8ta03784a.

[67] S.Q. Zhou, Y.T. Yang, W.Y. Zhang, X.F. Rao, P.X. Yan, T.T. Isimjan, X.L. Yang, Structure-regulated Ru particles decorated P-vacancy-rich CoP as a highly active and durable catalyst for $NaBH_4$ hydrolysis, J. Colloid Interface Sci. 591 (2021) 221–228, https://doi.org/10.1016/j.jcis.2021.02.009.

[68] J. Zhu, J. Chi, T. Cui, L. Guo, S. Wu, B. Li, J. Lai, L. Wang, F doping and P vacancy engineered FeCoP nanosheets for efficient and stable seawater electrolysis at large current density, Appl. Catal. B: Environ. 328 (2023), 122487, https://doi.org/10.1016/j.apcatb.2023.122487.

[69] T.L. Hui, C.L. Miao, J.T. Feng, Y.A. Liu, Q. Wang, Y.F. Wang, D.Q. Li, Atmosphere induced amorphous and permeable carbon layer encapsulating PtGa catalyst for selective cinnamaldehyde hydrogenation, J. Catal. 389 (2020) 229–240, https://doi.org/10.1016/j.jcat.2020.05.036.

[70] Y.T. Luo, Z.Y. Zhang, F.N. Yang, J. Li, Z.B. Liu, W.C. Ren, S. Zhang, B.L. Liu, Stabilized hydroxide-mediated nickel-based electrocatalysts for high-current-density hydrogen evolution in alkaline media, Energy Environ. Sci. 14 (2021) 4610–4619, https://doi.org/10.1039/d1ee01487k.

[71] C. Zhang, Y. Luo, J. Tan, Q. Yu, F. Yang, Z. Zhang, L. Yang, H.M. Cheng, B. Liu, High-throughput production of cheap mineral-based two-dimensional electrocatalysts for high-current-density hydrogen evolution, Nat. Commun. 11 (2020), 3724, https://doi.org/10.1038/s41467-020-17121-8.

[72] H.X. Yao, X.K. Wang, K. Li, C. Li, C.H. Zhang, J. Zhou, Z.W. Cao, H.L. Wang, M. Gu, M.H. Huang, H.Q. Jiang, Strong electronic coupling between ruthenium single atoms and ultrafine nanoclusters enables economical and effective hydrogen production, Appl. Catal. B: Environ. 312 (2022) 121378, https://doi.org/10.1016/j.apcatb.2022.121378.

[73] M. Maleki, A.S. Rouhaghdam, G.B. Darband, D. Han, S. Shanmugam, Highly active and durable NiCoSeP nanostructured electrocatalyst for large-current-density hydrogen production, ACS Appl. Energy Mater. 5 (2022) 2937–2948, https://doi.org/10.1021/acsaem.1c03625.

[74] K. Chi, Z. Wu, X. Tian, Z. Wang, F. Xiao, J. Xiao, S. Wang, Boosting hydrogen evolution via integrated construction and synergistic cooperation of confined graphene/$CoSe_2$ active interfaces and 3D graphene nanomesh arrays, Appl. Catal. B: Environ. 324 (2023), 122256, https://doi.org/10.1016/j.apcatb.2022.122256.

[75] Q. Li, F. Huang, S. Li, H. Zhang, X.Y. Yu, Oxygen vacancy engineering synergistic with surface hydrophilicity modification of hollow Ru doped CoNi-LDH nanotube arrays for boosting hydrogen evolution, Small 18 (2022), e2104323, https://doi.org/10.1002/smll.202104323.

[76] M.T. Jin, X. Zhang, R. Shi, Q. Lian, S.Z. Niu, O.W. Peng, Q. Wang, C. Cheng, Hierarchical CoP@Ni_2P catalysts for pH-universal hydrogen evolution at high current density, Appl. Catal. B: Environ. 296 (2021), 120350, https://doi.org/10.1016/j.apcatb.2021.120350.

[77] W.-B. Jung, G.-T. Yun, Y. Kim, M. Kim, H.-T. Jung, Relationship between hydrogen evolution and wettability for multiscale hierarchical wrinkles, ACS Appl. Mater. Interfaces 11 (2019) 7546–7552, https://doi.org/10.1021/acsami.8b19828.

[78] Q. Zhang, W. Xiao, W.H. Guo, Y.X. Yang, J.L. Lei, H.Q. Luo, N.B. Li, Macroporous array induced multiscale modulation at the surface/interface of $Co(OH)_2$/NiMo self-supporting electrode for effective overall water splitting, Adv. Funct. Mater. 31 (2021), 2102117, https://doi.org/10.1002/adfm.202102117.

[79] B.A. Yusuf, W. Yaseen, M. Xie, R.S. Zayyan, A.I. Muhammad, R. Nankya, J. Xie, Y. Xu, Recent advances in understanding and design of efficient hydrogen evolution electrocatalysts for water splitting: a comprehensive review, Adv. Colloid Interface Sci. (2022), 102811, https://doi.org/10.1016/j.cis.2022.102811.

[80] R. Miao, B. Dutta, S. Sahoo, J. He, W. Zhong, S.A. Cetegen, T. Jiang, S.P. Alpay, S. L. Suib, Mesoporous iron sulfide for highly efficient electrocatalytic hydrogen evolution, J. Am. Chem. Soc. 139 (2017) 13604–13607, https://doi.org/10.1021/jacs.7b07044.

[81] S. Jiao, X. Fu, H. Huang, Descriptors for the evaluation of electrocatalytic reactions: D-band theory and beyond, Adv. Energy Mater. 32 (2022), 2107651, https://doi.org/10.1002/adfm.202107651.

[82] C. Sun, P.C. Zhao, Y.Q. Yang, Z. Li, W.C. Sheng, Lattice oxygen-induced d-band shifting for enhanced hydrogen oxidation reaction on nickel, ACS Catal. 12 (2022) 11830–11837, https://doi.org/10.1021/acscatal.2c03264.

[83] B.G. Mao, P.P. Sun, Y. Jiang, T. Meng, D.L. Guo, J.W. Qin, M.H. Cao, Identifying the transfer kinetics of adsorbed hydroxyl as a descriptor of alkaline hydrogen evolution reaction, Angew. Chem. Int. Ed. 59 (2020) 15232–15237, https://doi.org/10.1002/anie.202006722.

[84] F. Kong, X. Liu, Y. Song, Z. Qian, J. Li, L. Zhang, G. Yin, J. Wang, D. Su, X. Sun, Selectively coupling Ru single atoms to PtNi concavities for high-performance methanol oxidation via d-band center regulation, Angew. Chem. Int. Ed. 61 (2022), e202207524, https://doi.org/10.1002/anie.202207524.

[85] C. Lv, X. Wang, L. Gao, A. Wang, S. Wang, R. Wang, X. Ning, Y. Li, D. W. Boukhvalov, Z. Huang, Triple functions of $Ni(OH)_2$ on the surface of WN nanowires remarkably promoting electrocatalytic activity in full water splitting, ACS Catal. 10 (2020) 13323–13333, https://doi.org/10.1021/acscatal.0c02891.

[86] S. Sarawutanukul, N. Phattharasupakun, M. Sawangphruk, 3D CVD graphene oxide-coated Ni foam as carbo-and electro-catalyst towards hydrogen evolution reaction in acidic solution: In situ electrochemical gas chromatography, Carbon 151 (2019) 109–119, https://doi.org/10.1016/j.carbon.2019.05.058.

[87] K. Ye, Z. Zhou, J. Shao, L. Lin, D. Gao, N. Ta, R. Si, G. Wang, X. Bao, In situ reconstruction of a hierarchical Sn-Cu/SnO_x core/shell catalyst for high-performance CO_2 electroreduction, Angew. Chem. Int. Ed. 59 (2020) 4814–4821, https://doi.org/10.1002/anie.201916538.

[88] H. Tian, X.Y. Li, L. Zeng, J.L. Gong, Recent advances on the design of group VIII base-metal catalysts with encapsulated structures, ACS Catal. 5 (2015) 4959–4977, https://doi.org/10.1021/acscatal.5b01221.

[89] W.Y. Jin, X.L. Guo, J. Zhang, L.K. Zheng, F. Liu, Y.C. Hu, J. Mao, H. Liu, Y.M. Xue, C.C. Tang, Ultrathin carbon coated CoO nanosheet arrays as efficient electrocatalysts for the hydrogen evolution reaction, Catal. Sci. Technol. 9 (2019) 6957–6964, https://doi.org/10.1039/C9CY01645G.